# Di-neutron correlation and soft dipole excitation in medium mass neutron-rich nuclei near drip line

Masayuki Matsuo, Kazuhito Mizuyama, and Yasuyoshi Serizawa
*Graduate School of Science and Technology, Niigata University, Niigata 950-2181, Japan*
(Received 13 August 2004; published 30 June 2005)

The neutron pairing correlation and the soft dipole excitation in medium mass nuclei near the drip line are investigated from the viewpoint of the di-neutron correlation. Numerical analyses based on the coordinate-space Hartree-Fock-Bogoliubov method and the continuum quasiparticle random phase approximation are performed for even-even $^{18-24}$O, $^{50-58}$Ca, and $^{80-86}$Ni. A clear signature of the di-neutron correlation is found in the ground state; two neutrons are correlated at short relative distances $\lesssim$2 fm with large probability $\sim$50%. The soft dipole excitation is influenced strongly by the neutron pairing correlation, and it accompanies a large transition density for pair motion of neutrons. This behavior originates from a coherent superposition of two-quasiparticle configurations $[l \times (l+1)]_{L=1}$ consisting of continuum states with high orbital angular momenta $l$ reaching an order of $l \sim 10$. It suggests that the soft dipole excitation under the influence of neutron pairing is characterized by the motion of di-neutron in the nuclear exterior against the remaining $A-2$ subsystem. Sensitivity to the density dependence of the effective pair force is discussed.

DOI: 10.1103/PhysRevC.71.064326 PACS number(s): 21.10.Ky, 21.10.Re, 21.60.Jz, 24.30.Cz

## I. INTRODUCTION

Excitations of neutron-rich nuclei near the drip line are subjects currently being investigated extensively. It is expected that exotic properties such as halo, skin, or presence of weakly bound nucleons in neutron-rich nuclei cause new features in excitations. An example is the soft dipole excitation in light halo nuclei [1–8], typically in $^{11}$Li and $^{11}$Be, where significant $E1$ strength is observed above the very low neutron threshold energy. This is in contrast to the situation in stable nuclei, where most of the $E1$ strength concentrates in the high energy region of giant resonances. Recently the soft dipole excitation has been observed also in heavier systems up to neutron-rich oxygen isotopes $^{18-22}$O [9,10]. These oxygen isotopes do not exhibit noticeable halo structure [11]; but on the other hand, they contain many valence neutrons. This suggests that the soft dipole excitation is not always inherent in a one- or two-neutron halo, but instead it may be a many-body phenomenon more generally seen in many neutron-rich nuclei near the drip line reaching medium mass and possibly heavier regions.

The degree of collectivity or the nature of correlations responsible for this excitation is one of the central issues that need to be clarified. Indeed, different mechanisms have been proposed so far. One of the simplest mechanisms producing the soft dipole excitation is the one associated with uncorrelated excitation of a weakly bound neutron to continuum states. In this case, significant $E1$ strength emerges just above the threshold energy of neutron escaping without resorting to correlations or collectivity; it is sometimes called the threshold effect [12,13]. This arises from a large spatial overlap between the extended wave function of a weakly bound single-particle orbit, which is occupied by a neutron in the ground state, and that of low energy continuum orbits, to which the neutron is excited. Major aspects of the soft dipole excitation observed in one-neutron halo systems, e.g., $^{11}$Be, fit rather well with this uncorrelated excitation picture [4,5]. However, when more than one neutron participates in the excitation, correlation between neutrons plays a role, and different mechanisms of the soft dipole excitation can be expected. In the case of the two-neutron halo nucleus $^{11}$Li, the pairing correlation among halo neutrons plays a decisive role for the binding and formation of the halo [14–18]. It is suggested that the two halo neutrons in the ground state display an attractive correlation in such a way that they are spatially localized with respect to their relative distance, in a range smaller than the size of the nuclear matter radius [14,16,17]. The spatial localization of the correlated pair has been discussed also in stable closed-shell core plus two-neutron systems [19–22]. The pairing correlation of this type or the di-neutron correlation in short is predicted to cause a strong enhancement of the soft dipole excitation in the two-neutron halo nucleus [14,23,24], or even to form a collective vibrational motion of the correlated halo neutrons against the rest of the system [15,25].[1] Experimentally, signatures of a possible di-neutron correlation in the soft dipole excitation are obtained in $^{11}$Li [2], but strong neutron-neutron correlations are not probed in other experiments [1,3].

The soft dipole excitation in medium mass nuclei has also been investigated theoretically, but with different viewpoints and results. The random phase approximation (RPA) calculations based on the Hartree-Fock models or the relativistic mean-field model predict that the soft dipole excitations have a character of uncorrelated neutron excitation carrying very little collectivity in the neutron-rich oxygen isotopes [25–27].

[1]The collective vibrational mode of halo neutrons predicted by Ref. [15] is called the soft dipole mode or the soft dipole resonance. The term soft dipole excitation, on the other hand, is sometimes used to distinguish from this picture or to emphasize a picture of uncorrelated excitation of halo neutrons. In the present paper, however, we use the soft dipole excitation only to imply neutrally an excitation carrying a significant $E1$ strength far below the giant dipole resonance energy without specifying any other characters.

 

Note, however, that these RPA models do not take into account the pair correlations among neutrons. The shell model calculation [28] reproduces rather well the experimental soft dipole strength in oxygen isotopes, but continuum effects are not included. Recently quasiparticle RPA (QRPA) calculations that include explicitly the neutron pairing corrections have been performed [29–34]. It is predicted that the neutron pair correlation has a sizable effect on $E1$ strength of the soft dipole excitation in the oxygen isotopes [31,32]. This suggests that the neutron pair correlation is an important key to clarifying the character of the soft dipole excitation in medium mass and heavier systems.

In the present paper, we analyze in detail pair correlation effects in the medium mass region with $Z = 8-28$, taking proton (semi-) magic oxygen, calcium, and nickel isotopes as representative examples. Motivated by the debate on the light two-neutron halo nuclei, we pay special attention to possibilities of the di-neutron correlation also in these medium mass nuclei. We will conclude that some features of the di-neutron correlation are indeed present rather generally in the ground state of the medium mass nuclei. Furthermore the di-neutron correlation also brings about a characteristic and strong influence on the soft dipole excitation.

Our analysis is based on the Hartree-Fock-Bogoliubov (HFB) method in the coordinate-space representation for description of the ground state, and the continuum quasiparticle random phase approximation (the continuum QRPA) for the excitations. The coordinate-space HFB theory [35,36] has been applied to describe the pair-correlated ground state in near-drip-line nuclei as weakly bound and continuum orbits are treated precisely through an explicit account of the coordinate dependence of the pair potential and the quasiparticle wave functions [37–43]. Generalization of the HFB theory to a time-dependent problem, i.e., a linear response against an external perturbation, leads to the quasiparticle random phase approximation (QRPA) [44,45]. Thus, QRPA methods that build upon the HFB ground states [31,33,46–52] as well as similar approaches formulated on the relativistic mean-field Bogoliubov models [32,53,54] have been developed recently to describe excitation modes in medium mass and heavier neutron-rich nuclei. We note here that the soft dipole excitation has a special aspect in that the $E1$ strength associated with this excitation is embedded and broadly distributed in the continuum energy region just above the threshold energy of neutron escaping. In fact, most of the soft dipole strength observed in the oxygen isotopes lies above the threshold without forming a narrow resonance [9], implying considerable neutron escaping from this excitation mode. It is therefore important to treat precisely escaping neutrons within the QRPA framework. This is what the continuum QRPA methods achieve [48,49]. In the present work, we use our own formulation of the continuum QRPA [48], and apply it to the soft dipole excitation. An important feature of this formulation is that it utilizes the exact quasiparticle Green function satisfying the proper out going boundary condition for neutrons. (In this respect, it is an extension of the continuum RPA [26,55,56] which, however, neglects the pair correlation.) Accordingly, the theory enables us to take into account pair correlation acting among escaping neutrons, which will be important for formation of a di-neutron correlation in the dipole excitation. Since the pair correlations are focused in the present analysis, we perform calculations satisfying the self-consistency in the particle-particle channel (the pairing channel) by using the self-consistent HFB pair potential and the residual pair interaction derived from a single effective pairing force. Concerning the particle-hole channel, we use a Woods-Saxon potential and a residual interaction of a delta force type, violating the self-consistency in this channel. Finally we note that as our approach is fully microscopic in treating all the nucleon degrees of freedom democratically, the di-neutron correlation, if present, emerges only as a consequence of the microscopic description. To probe the di-neutron behaviors in the ground state and in the soft dipole excitation, we look into the two-body correlation density and the pair transition densities, which provide information on pair motion of neutrons.

Numerical calculations are performed for even-even neutron-rich oxygen, calcium, and nickel isotopes $^{18-24}$O, $^{50-58}$Ca, and $^{80-86}$Ni near the drip line and for some more stable isotopes for comparison. In Sec. II, we analyze the di-neutron correlation in the ground state. In Sec. III, analysis of the soft dipole excitations using the continuum QRPA method is presented. Conclusions are drawn in Sec. IV. We do not discuss in the present paper the low-lying dipole strength in stable nuclei with neutron excess, called pygmy dipole resonance [57–61], because the situations are different from those in near-drip-line nuclei on which we focus the present paper. A preliminary report of the present work is seen in Ref. [62].

## II. DI-NEUTRON CORRELATION IN THE GROUND STATE

### A. Coordinate-space HFB with density-dependent interaction

Wave functions of weakly bound neutrons in nuclei close to the drip line extend largely to the outside of the nuclear surface because of the quantum mechanical penetration. Since associated neutron density is very low, the pair correlations in internal, surface, and external regions may be different. The coordinate-space Hartree-Fock-Bogoliubov theory [35–37] enables us to deal with this nonuniformity by utilizing an explicit coordinate representation for the Bogoliubov quasiparticles, which are the fundamental modes of the single-particle motion under the influence of a pairing correlation. In this scheme, the quasiparticles are able to have both particle and hole characters simultaneously, and accordingly they are expressed by the two-component wave functions

$$\phi_{iq}(\boldsymbol{r}\sigma) \equiv \begin{pmatrix} \varphi_{1,iq}(\boldsymbol{r}\sigma) \\ \varphi_{2,iq}(\boldsymbol{r}\sigma) \end{pmatrix}, \tag{1}$$

where $\sigma = \pm\frac{1}{2} = \uparrow, \downarrow$, and $q = n, p$ represent spin and isospin. The quasiparticle states are determined by the HFB equation

$$\mathcal{H}_{0q}\phi_{iq}(\boldsymbol{r}\sigma) = E_{iq}\phi_{iq}(\boldsymbol{r}\sigma), \tag{2}$$

with

$$\mathcal{H}_{0q} = \begin{pmatrix} h_q - \lambda_q & \tilde{h}_q \\ \tilde{h}_q & -h_q + \lambda_q \end{pmatrix}, \tag{3}$$

where $E_{iq}$ is the quasiparticle energy. The HFB self-consistent mean-field Hamiltonian $\mathcal{H}_{0q}$ consists of not only the particle-hole part $h_q - \lambda_q$ including the kinetic energy term, the Hartree-Fock mean field, and the Fermi energy $\lambda_q$, but also the particle-particle part $\tilde{h}_q$ originating from the pair correlation. The mean-field Hamiltonian, $h_q$ and $\tilde{h}_q$, are expressed in terms of the normal density matrix $\rho_q(\boldsymbol{r}\sigma, \boldsymbol{r}'\sigma') = \langle\Phi_0|\,\psi_q^\dagger(\boldsymbol{r}'\sigma')\psi_q(\boldsymbol{r}\sigma)\,|\Phi_0\rangle$, the pair density matrix $\tilde{\rho}_q(\boldsymbol{r}\sigma, \boldsymbol{r}'\sigma') = \langle\Phi_0|\,\psi_q(\boldsymbol{r}'\tilde{\sigma}')\psi_q(\boldsymbol{r}\sigma)\,|\Phi_0\rangle = (-2\sigma')\,\langle\Phi_0|\,\psi_q(\boldsymbol{r}' - \sigma')\psi_q(\boldsymbol{r}\sigma)\,|\Phi_0\rangle$, and the effective nuclear force. We do not need the explicit form of the correlated HFB ground state $|\Phi_0\rangle$ since ground state expectation values of various physical quantities can be evaluated with use of the Wick's theorem for the quasiparticle annihilation and creation operators $\beta_{iq}$ and $\beta_{iq}^\dagger$ satisfying the vacuum condition $\beta_{iq}\,|\Phi_0\rangle = 0$, and with use of their relation to the nucleon annihilation and creation operators given by

$$\begin{aligned} \psi_q(\boldsymbol{r}\sigma) &= \sum_i \varphi_{1,iq}(\boldsymbol{r}\sigma)\beta_{iq} - \varphi_{2,iq}^*(\boldsymbol{r}\tilde{\sigma})\beta_{iq}^\dagger, \\ \psi_q^\dagger(\boldsymbol{r}\sigma) &= \sum_i \varphi_{1,iq}^*(\boldsymbol{r}\sigma)\beta_{iq}^\dagger - \varphi_{2,iq}(\boldsymbol{r}\tilde{\sigma})\beta_{iq}. \end{aligned} \tag{4}$$

In the present work, we derive the particle-particle mean-field $\tilde{h}_q$ by using the self-consistent HFB scheme. As the effective nuclear force responsible for the particle-particle part $\tilde{h}_q$, called the effective pairing force below, we adopt the density-dependent delta interaction [14,63,64]

$$v_{\rm pair}(\boldsymbol{r}, \boldsymbol{r}') = \frac{1}{2}V_0(1 - P_\sigma)\left[1 - \frac{\rho(\boldsymbol{r})}{\rho_0}\right]\delta(\boldsymbol{r} - \boldsymbol{r}'). \tag{5}$$

With this choice, the particle-particle part $\tilde{h}_q$ becomes a local pair potential $\Delta_q(\boldsymbol{r}) = \frac{V_0}{2}[1 - \frac{\rho(\boldsymbol{r})}{\rho_0}]\tilde{\rho}_q(\boldsymbol{r})$ expressed with the diagonal pair density $\tilde{\rho}_q(\boldsymbol{r}) = \sum_\sigma \tilde{\rho}_q(\boldsymbol{r}\sigma, \boldsymbol{r}\sigma)$. The parameter $\rho_0$ together with the total density $\rho(\boldsymbol{r}) = \rho_n(\boldsymbol{r}) + \rho_p(\boldsymbol{r})$ in Eq. (5) controls the density dependence of the effective pairing force. There is no established knowledge on the density dependence of the pairing force, being under current investigations [38,39,65]. In the following analysis, we consider three cases: (1) the pairing with strong density dependence (or the surface pairing force for short) for which the parameter $\rho_0$ is set to the central total density $\rho_0 = 0.19$ fm$^{-3}$, (2) the density-independent pairing force with the choice of $1/\rho_0 = 0$ (the volume pairing force), and (3) the case of an intermediate density dependence with $\rho_0 = 0.32$ fm$^{-3}$ (the mixed pairing force). Since a recent analysis suggests that the mixed pairing force reproduces better the odd-even mass difference in many isotopic chains [39], we adopt the mixed pairing as a reference choice. The surface and volume pairing forces are employed to examine sensitivity to the density dependence.

Concerning the particle-hole part $h_q$ of the HFB Hamiltonian, it is in principle possible to derive it by using an effective interaction, e.g., the Skyrme force, as we have a code to calculate the HFB ground state and the static HFB mean fields. On the other hand, we are not yet ready to apply the full Skyrme force to the continuum QRPA method [48] utilizing the exact Green function with the outgoing boundary condition. In the present analysis, therefore, we replace $h_q$ by a spherical Woods-Saxon potential model both in the HFB and the continuum QRPA calculations. It should be examined, of course, how choices of the particle-hole mean field affect numerical results. This point is briefly discussed below in reference to the pair correlation in the ground states. The parameters of the Woods-Saxon model follow Ref. [55], which gives a reasonable description of the giant dipole excitation in doubly shell-closed stable nuclei, such as $^{16}$O and $^{40}$Ca. Neutron single-particle orbits near the Fermi energy are shown in Fig. 1 for representative isotopes.

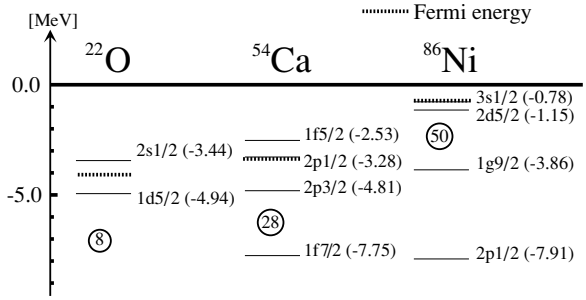


FIG. 1. Woods-Saxon single-particle levels of neutrons in $^{22}$O,$^{54}$Ca, and $^{86}$Ni. The single-particle energy is indicated in parenthesis. The thick dotted line is the calculated Fermi energy.

Assuming the spherical symmetry, we solve the HFB Eq. (2) in the radial coordinate for each partial wave. Here we adopt the radial mesh size $\Delta r = 0.2$ fm, and the box size $r_{\rm max} = 20$ fm. To achieve self-consistency between the quasiparticle wave functions and the HFB pair potential, an iteration method [35] is used. As the contact interaction is adopted as the effective pair force, we need an energy cutoff, which is done here with respect to the quasiparticle energy bounded by the maximum limit $E_{\rm max}$. We adopt a value $E_{\rm max} = 50$ MeV following the arguments in Refs. [35,37]. Similarly large values are adopted in many recent HFB and HFB+QRPA calculations [38–43,49–51,65]. We include all the quasiparticle states under the energy cutoff and another cutoff for the orbital angular momentum $l$ of the quasiparticle states: we adopt a large value $l_{\rm max} = 12$ to give good convergence. Note that the space contains neutron quasiparticle states in the continuum energy region $E > |\lambda_q|$ lying above the threshold $|\lambda_q|$. We shall discuss roles of high-lying and high-$l$ quasiparticle states in the following section.

The force strength parameter $V_0$ in Eq. (5) is fixed for each isotope chain so that the calculated neutron average gap $\langle\Delta_n\rangle = \int \tilde{\rho}_n(\boldsymbol{r})\Delta_n(\boldsymbol{r})d\boldsymbol{r} / \int \tilde{\rho}_n(\boldsymbol{r})d\boldsymbol{r}$ [35,48,66] gives an overall agreement with the odd-even mass difference of the three-point formula [67], as shown in Fig. 2. A common value $V_0 = -280$ MeV fm$^3$ is adopted in the case of the mixed pairing. Note that we here improve the pairing force parameter, compared with our previous calculations [31,48] where the conventional systematics $\Delta_{\rm syst} = 12/\sqrt{A}$ MeV is

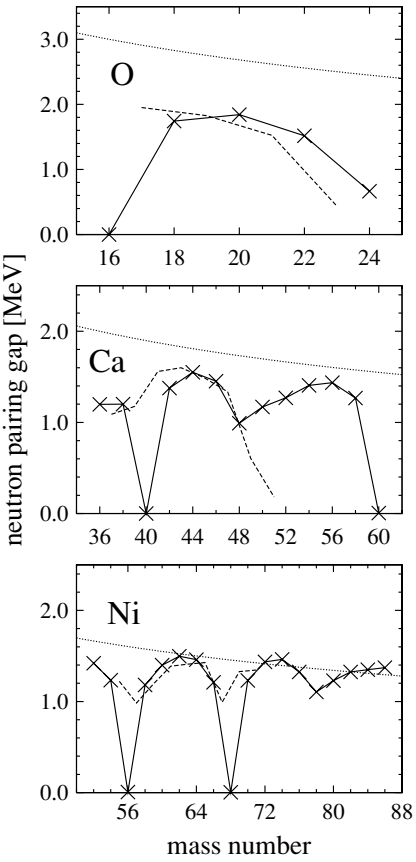


FIG. 2. Calculated neutron average pairing gap $\langle\Delta_n\rangle$ in O, Ca, and Ni isotopes, plotted with crosses. Experimental odd-even mass difference evaluated with the three-point formula [67] is shown by dashed line. Dotted line is the conventional systematics $\Delta_{\rm syst} = 12/\sqrt{A}$ MeV of the pairing gap.

fitted to determine $V_0$. The value of $\Delta_{\rm syst}$ in the oxygen isotopes is larger by about 40% than the experimental odd-even mass difference (Fig. 2).

### B. Two-body correlation density

To analyze the spatial behavior of the neutron pair correlation and to search for possible di-neutron aspects, we evaluate the two-body correlation density

$$\rho_{{\rm corr},q}(\boldsymbol{r}\sigma,\boldsymbol{r}'\sigma') = \langle\Phi_0|\sum_{i\neq j\in q}\delta(\boldsymbol{r}-\boldsymbol{r}_i)\delta(\boldsymbol{r}'-\boldsymbol{r}_j)\delta_{\sigma_i\sigma}\delta_{\sigma_j\sigma'}|\Phi_0\rangle - \rho_q(\boldsymbol{r}\sigma)\rho_q(\boldsymbol{r}'\sigma') \quad (6)$$

for the calculated ground state. This quantity displays a correlation between two neutrons at positions $\boldsymbol{r}$ and $\boldsymbol{r}'$ with spins $\sigma$ and $\sigma'$. The spin antiparallel (spin-singlet) configuration $\sigma\sigma' = \uparrow\downarrow$ is responsible for the neutron pairing. In the above definition, we subtract the uncorrelated contribution $\rho_q(\boldsymbol{r}\sigma)\rho_q(\boldsymbol{r}'\sigma')$ in order to separate the change originating from the correlation.

Using the creation-annihilation operators and Wick's theorem, the two-body correlation density is expressed as

$$\begin{aligned}\rho_{{\rm corr},q}(\boldsymbol{r}\sigma,\boldsymbol{r}'\sigma') &= \langle\Phi_0|\psi_q^\dagger(\boldsymbol{r}\sigma)\psi_q^\dagger(\boldsymbol{r}'\sigma')\psi_q(\boldsymbol{r}'\sigma')\psi_q(\boldsymbol{r}\sigma)|\Phi_0\rangle \\ &\quad - \rho_q(\boldsymbol{r}\sigma)\rho_q(\boldsymbol{r}'\sigma') \\ &= |\tilde\rho_q(\boldsymbol{r}\sigma,\boldsymbol{r}'\tilde\sigma')|^2 - |\rho_q(\boldsymbol{r}\sigma,\boldsymbol{r}'\sigma')|^2, \end{aligned} \quad (7)$$

in terms of off-diagonal parts of the pair and the normal density matrices. For the spin antiparallel configuration, the last term of Eq. (7) gives only a minor contribution, while it gives the Pauli repulsion correlation for the spin parallel configuration. In the following, we concentrate on the spin antiparallel neutron correlation. In displaying this quantity, we fix the position $\boldsymbol{r}'$ of one spin-down ($\sigma' = \downarrow$) neutron (called the reference neutron hereafter) and plot it as a function of the position $\boldsymbol{r}$ of the other spin-up ($\sigma = \uparrow$) neutrons. Actual plots are made for the two-body correlation density $\rho_{{\rm corr},n}(\boldsymbol{r}\uparrow,\boldsymbol{r}'\downarrow)/\rho_n(\boldsymbol{r}'\downarrow)$ divided by the neutron density $\rho_n(\boldsymbol{r}'\downarrow)$ at the position of the reference neutron. This represents the conditional probability of finding neutrons at position $\boldsymbol{r}$ with spin $\sigma = \uparrow$ provided that the reference neutron is fixed at $\boldsymbol{r}'$ with spin $\sigma' = \downarrow$. This normalization removes the trivial radial dependence of the density that falls off exponentially as the reference neutron position moves to the exterior region. This facilitates comparison among different positions of the reference neutron.

Examples of the two-body correlation density are displayed in Fig. 3 for nuclei near the drip line $^{22}$O, $^{58}$Ca, and $^{84}$Ni. The reference neutron is placed at a position $\boldsymbol{r}' = (0, 0, z')$ along the $z$ axis, where $z'$ is fixed at the surface radius $z' = R_{\rm surf}$. We evaluate $R_{\rm surf}$ by a position of the half central neutron density. To examine dependence on the reference neutron position, it is further displaced at an internal ($z' = R_{\rm surf} - 2$ fm) and an external ($z' = R_{\rm surf} + 2$ fm) positions shifted by $\pm 2$ fm from the surface. The external position $z' = R_{\rm surf} + 2$ fm represents the neutron skin region, as the neutron density at this position is about $\sim 1/30$ of the central density (see later in Fig. 6) in these isotopes. (Note that a criterion $\rho_n(\boldsymbol{r})/\rho_n(0) = 1/100$ is sometimes adopted in the literature [68,69] to define the neutron skin thickness and to distinguish from a typical neutron halo, which emerges with a lower density $\rho_n(\boldsymbol{r})/\rho_n(0) < 1/100$.)

It is seen that the correlation density $\rho_{{\rm corr},n}(\boldsymbol{r}\uparrow,\boldsymbol{r}'\downarrow)$ exhibits a large and sharp peak in all the cases shown in Fig. 3. The peak position almost coincides with the reference neutron position. The distribution is concentrated mostly within an interval $\lesssim 2-3$ fm around the peak. The peak width $\xi_d$, evaluated by the full width at half maximum (FWHM), reads only about 2 fm when the reference neutron is placed at the internal or the surface positions, whereas the spreading of the peak becomes slightly wider in the case of the external position. This obviously means a strong concentration of the correlation density around the reference neutron as the width $\xi_d$ is smaller than the nuclear radius or the distance between the reference neutron and the nuclear center. In the region other than the first largest peak, the correlation density displays oscillatory behaviors, but its absolute value is much smaller than the first largest peak. The observed concentration of the

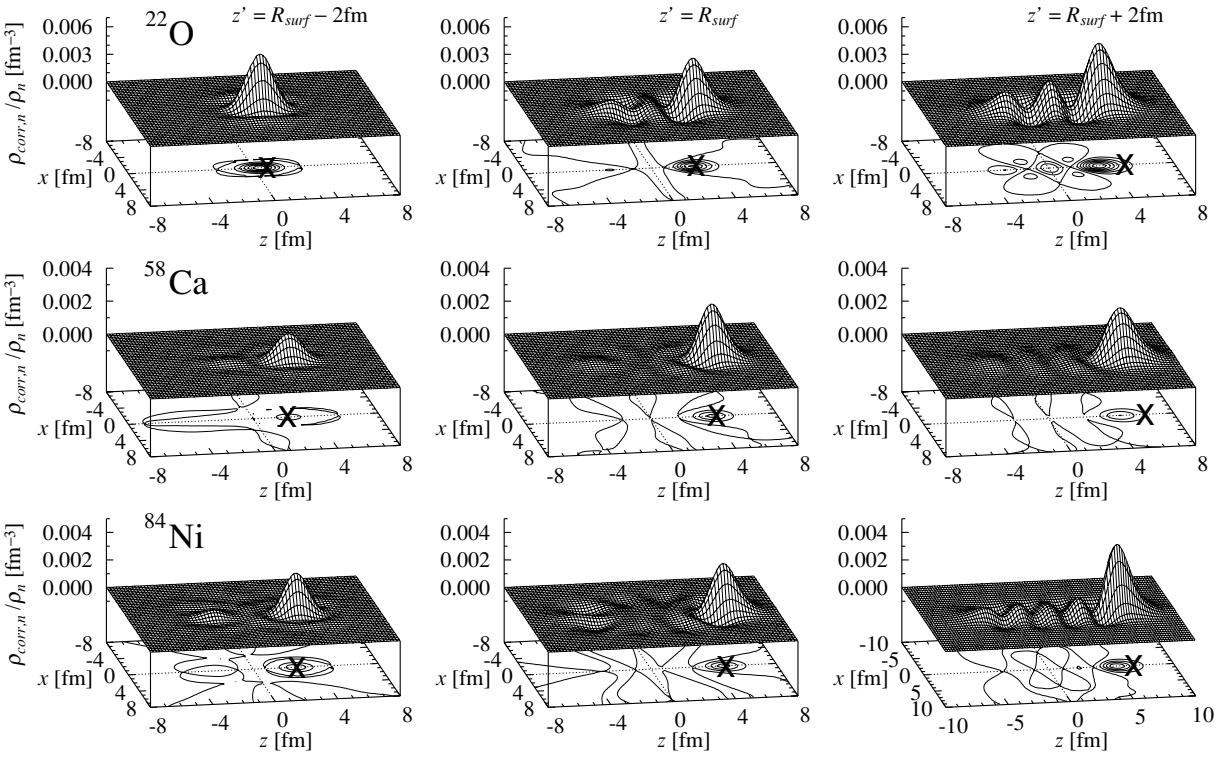


FIG. 3. Neutron two-body correlation density $\rho_{\mathrm{corr},n}(\boldsymbol{r}\uparrow, \boldsymbol{r}'\downarrow)/\rho_n(\boldsymbol{r}'\downarrow)$ in $^{22}$O, $^{58}$Ca, and $^{84}$Ni calculated with the mixed pairing force is drawn on the $x$-$z$ plane. A contour plot of the same quantity is attached in the bottom of each panel where the interval of contour lines is 0.001 fm$^{-3}$. The symbol "X" on the $x$-$z$ plane indicates the position $\boldsymbol{r}' = (0, 0, z')$ of the reference neutron. Results for $^{22}$O, $^{58}$Ca, and $^{84}$Ni are listed in the top, middle, and bottom rows, respectively. In the middle column, the reference neutron is fixed at the nuclear surface $z' = R_{\mathrm{surf}}$, whereas it is placed at the external position $z' = R_{\mathrm{surf}} + 2.0$ fm in the right column and at the internal position $z' = R_{\mathrm{surf}} - 2.0$ fm in the left column. See Table I for the value of $R_{\mathrm{surf}}$.

two-body correlation density in the small region around the reference neutron indicates that two neutrons with the spin antiparallel (spin singlet) configuration have a large probability of coming close at short relative distances $|\boldsymbol{r} - \boldsymbol{r}'| \lesssim 2{-}3$ fm. It may be possible to regard this feature of the neutron pairing as that of the di-neutron correlation. This di-neutron correlation resembles qualitatively the spatial localization of correlated two neutrons suggested in the previous studies of two-neutron halo nuclei [14,16,17] and of stable nuclei having closed-shell core plus two neutrons [19–22].

It is possible to quantify the extent of the di-neutron correlation by evaluating the first largest peak in the two-body correlation density. Here we note that the second last term in Eq. (7), expressed in terms of the pair density matrix $\tilde{\rho}_n$, gives the dominant contribution to the correlation density. It is customary to regard the pair density matrix $\tilde{\rho}_n(\boldsymbol{r}\sigma, \boldsymbol{r}'\tilde{\sigma}') = \langle\Phi_0|\psi_n(\boldsymbol{r}\sigma)\psi_n(\boldsymbol{r}'\sigma')|\Phi_0\rangle$ as the wave function of a neutron pair in the correlated ground state. In this sense, the second last term $|\tilde{\rho}_n(\boldsymbol{r}\sigma, \boldsymbol{r}'\tilde{\sigma}')|^2 \equiv p_n(\boldsymbol{r}\sigma, \boldsymbol{r}'\sigma')$ with the opposite spins represents the probability distribution of a spin-singlet neutron pair. Using this quantity and normalizing, we can define a relative probability

$$p(r_d) = \frac{\int_{|\boldsymbol{r}-\boldsymbol{r}'|<r_d} p_n(\boldsymbol{r}\uparrow, \boldsymbol{r}'\downarrow)d\boldsymbol{r}}{\int p_n(\boldsymbol{r}\uparrow, \boldsymbol{r}'\downarrow)d\boldsymbol{r}} \tag{8}$$

for the spin-up neutron to exist within a distance $r_d$ from the spin-down reference neutron. The quantity $p(r_d)$ with a suitable value of $r_d$ measures the probability for the correlated neutron pair to form the di-neutron peak. We call it the di-neutron probability in the following. Calculated examples of the di-neutron probability are listed in Table I. We adopt $r_d = 2$ fm for the internal and the surface cases; while for

TABLE I. Di-neutron probability $p(r_d)$ in $^{22}$O, $^{58}$Ca, and $^{84}$Ni near the neutron drip line, and in more stable $^{44}$Ca and $^{66}$Ni. The reference neutron position $\boldsymbol{r}' = (0, 0, z')$ is fixed at the surface ( $z' = R_{\mathrm{surf}}$ ), internal ($z' = R_{\mathrm{surf}} - 2$ fm), and external ($z' = R_{\mathrm{surf}} + 2$ fm) positions. The surface radius $R_{\mathrm{surf}}$ defined by the half central density of neutrons is also listed. The di-neutron probability is evaluated with $r_d = 2$ fm except in the external case, where we use $r_d = 3$ fm. See also the text.

| | $R_{\mathrm{surf}}$ (fm) | $p(r_d)$ | | |
|---|---|---|---|---|
| | | Internal | Surface | External |
| $^{22}$O | 2.9 | 0.32 | 0.48 | 0.47 |
| $^{58}$Ca | 4.2 | 0.39 | 0.53 | 0.59 |
| $^{84}$Ni | 4.8 | 0.32 | 0.49 | 0.47 |
| $^{44}$Ca | 3.6 | 0.44 | 0.46 | 0.51 |
| $^{66}$Ni | 4.3 | 0.36 | 0.51 | 0.48 |

the external case, $r_d = 3$ fm is chosen to cover the large peak near the reference neutron (cf. Fig. 3, and later Figs. 7 and 8). The di-neutron probability amounts to 30–60%. As a reference, we compare with an estimate that would be obtained if the neutron pair probability $p_n(\boldsymbol{r}\uparrow, \boldsymbol{r}'\downarrow)$ were distributed uniformly in the whole nuclear volume. This uniform limit, which we evaluate by replacing $p_n(\boldsymbol{r}\uparrow, \boldsymbol{r}'\downarrow)$ with the neutron density $\rho_n(\boldsymbol{r})$, gives $p(r_d) = 0.20, 0.10, 0.06$ for $z' = R_{\rm surf} - 2, +0, +2$ fm in $^{22}$O, 0.08, 0.04, 0.03 in $^{58}$Ca, and 0.05, 0.03, 0.02 in $^{84}$Ni. In contrast to the uniform limit, the microscopically calculated values of $p(r_d)$ shown in Table I exhibit a significant enhancement especially at the surface and external positions.

The di-neutron correlation emerges systematically at different positions inside and outside the nucleus, as seen in Fig. 3. Inspecting in more detail, we find that, besides the width mentioned above, features of the di-neutron correlation vary with the reference neutron position. When the reference neutron is moved from the internal position ($z' = R_{\rm surf} -$ 2 fm) to the surface ($z' = R_{\rm surf}$), the di-neutron correlation apparently enhances. This is also seen in the di-neutron probability (see the cases of $^{22}$O, $^{58}$Ca, and $^{84}$Ni in Table I), which shows an increase from $p(r_d) \approx 30{-}40\%$ at the internal position to $\approx$50% at the surface position. Moving further toward the outside, as represented by the external position in the skin region $z' = R_{\rm surf} + 2$ fm, the concentration of correlation density around the largest peak is constantly quite large, keeping the di-neutron probability $p(r_d) \approx 50{-}60\%$. It is seen in this case that the peak position of the correlation density deviates slightly from the reference neutron position. The deviation is, however, within the di-neutron width $\xi_d$, keeping a large spatial overlap of the other neutron with the reference one. As the reference neutron moves far outside the nucleus, the deviation from the reference neutron increases further whereas the spatial correlation survives rather robustly even around $z' \sim R_{\rm surf} + 3$ to $+4$ fm in $^{58}$Ca and $^{84}$Ni. (An example of the correlation density with $z' = R_{\rm surf} + 3$ fm is shown in Fig. 4.) This behavior also manifests itself in the pair probability $p(r_d)$. In $^{58}$Ca, for example, this quantity with the reference neutron positions $z' = R_{\rm surf} + 2, +3, +4$ and $+5$ fm reads $p(r_d) = 0.59, 0.57, 0.52$, and 0.53 with $r_d =$ 3, 4, 5, and 6 fm chosen respectively, to encompass the first largest peak, whereas $p(r_d)$ with fixed $r_d$(=3 fm) decreases as $p(r_d) = 0.59, 0.38, 0.18, 0.07$ at the same reference positions. We find a similar behavior in $^{84}$Ni, while in $^{22}$O the strong concentration of two-body correlation density is seen for $z' \lesssim R_{\rm surf} + 3$ fm. These observations indicate that the di-neutron correlation is most strong in the surface and the skin regions while the spatial correlation associated with the di-neutron behavior remains and decreases only gradually even outside the skin.

If we compare the oxygen, calcium, and nickel isotopes in Fig. 3, we observe that the concentration of two-body correlation density around the position of reference neutron is more evident in $^{58}$Ca and $^{84}$Ni than in $^{22}$O. For example, the di-neutron probability in $^{58}$Ca and $^{84}$Ni is as large as the one in $^{22}$O (Table I). This means that the enhancement relative to the uniform limit is much larger in $^{58}$Ca and especially in $^{84}$Ni than in $^{22}$O. It is also seen that the oscillatory

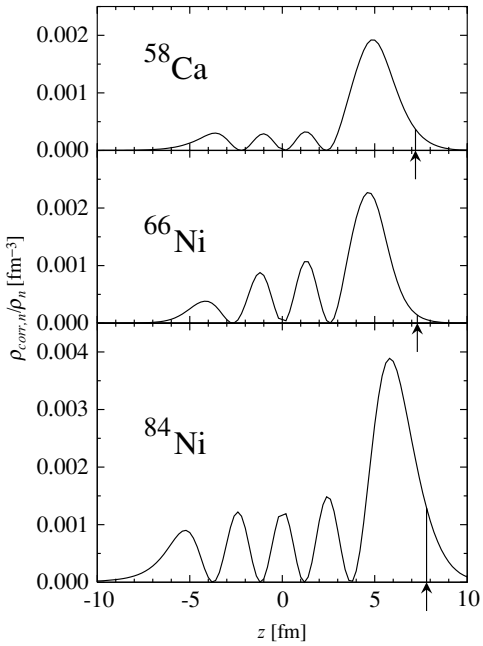


FIG. 4. Neutron two-body correlation density evaluated along the $z$ axis in the near-drip-line nuclei $^{58}$Ca and $^{84}$Ni, and in a more stable isotope $^{66}$Ni. Reference neutron is fixed at $z' = R_{\rm surf} + 3$ fm, as indicated by arrows.

behavior apart from the largest peak is weaker in $^{58}$Ca and $^{84}$Ni than in $^{22}$O, especially when the reference neutron is placed at the external position. The small oscillation is a remnant of nodal structure in the wave functions of neutron single-quasiparticle states near the Fermi energy, e.g., $2s_{1/2}$ and $1d_{5/2,3/2}$ neutron states in the case of $^{22}$O, although the magnitude of oscillation is suppressed by coherent contributions of other neutron quasiparticle states (see the next subsection for details). The smearing of the single-particle structures is more effective in heavier systems as more single-particle levels participate in the pairing correlation. It should be noted also that the neutron separation energy (related to the Fermi energy) is smaller in $^{58}$Ca and especially in $^{84}$Ni than in $^{22}$O (see Fig. 1). This difference in neutron binding also influences the neutron pairing correlation in the external region as discussed just below.

We have also analyzed the neutron two-body correlation density along the isotopic chains of Ca and Ni to check the di-neutron property in more stable nuclei and to examine how the di-neutron correlation varies with an approaching neutron drip line. We select $^{44}$Ca and $^{66}$Ni as examples representing stable nuclei and neutron-rich unstable nuclei (situated between the drip line and the stable region), respectively. Here $^{66}$Ni is chosen to compare with the near-drip-line nucleus $^{58}$Ca having the same neutron number $N = 38$ and with the near-drip-line isotope $^{84}$Ni. It is found that the gross behavior of the two-body correlation density in $^{44}$Ca and $^{66}$Ni is similar to those in $^{58}$Ca and $^{84}$Ni in the surface and the internal regions. As a representative example, we show in Fig. 5 the two-body correlation density in $^{44}$Ca and $^{66}$Ni for the reference neutron fixed at the surface ($z' = R_{\rm surf}$). In Table I, we do not see an obvious difference between the near-drip-line nuclei and the more

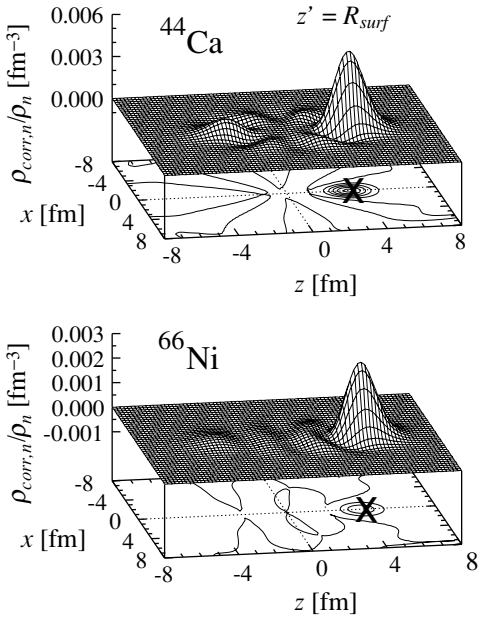


FIG. 5. Same as Fig. 3, but for $^{44}$Ca and $^{66}$Ni. Reference neutron is fixed at the surface position $z' = R_{\rm surf}$.

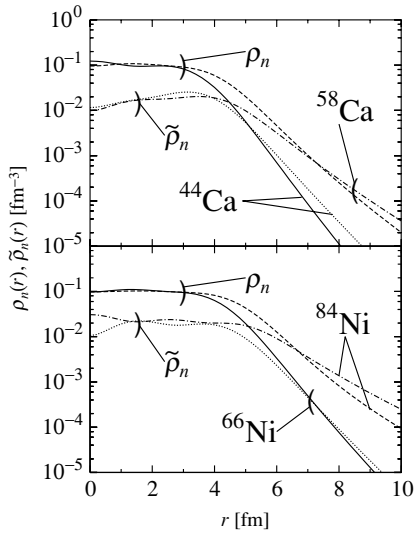


FIG. 6. Density $\rho_n(r)$ and pair density $\tilde{\rho}_n(r)$ of neutrons in $^{44,58}$Ca and $^{66,84}$Ni. Solid and dashed lines represent $\rho_n(r)$; dotted and dot-dashed lines are for $\tilde{\rho}_n(r)$.

stable ones in the di-neutron probabilities $p(r_d)$ at the internal position $z' = R_{\rm surf} - 2$ fm and at the surface $z' = R_{\rm surf}$.

A clear difference emerges, however, when the reference neutron is placed far outside the nuclear surface. This is illustrated by Fig. 4, where we compare the correlation densities in $^{66}$Ni, $^{84}$Ni, and $^{58}$Ca with a reference neutron fixed at a position ($z' = R_{\rm surf} + 3$ fm) in the far outside region. The value of the correlation density evaluated at the reference neutron position is lower in $^{66}$Ni by a factor of 2 or more than in the near-drip-line nuclei $^{58}$Ca and $^{84}$Ni. Moreover, the large correlation density at the position of the reference neutron is most significant in $^{84}$Ni. This indicates that the di-neutron correlation in the external region is stronger in near-drip-line nuclei having shallower neutron Fermi energy than that in more stable nuclei with deeper Fermi energy (see Fig. 1 for the single-particle energies and the Fermi energy in these nuclei). We can also see this property directly in the profiles of the pair density $\tilde{\rho}_n(r)$ of neutrons, shown in Fig. 6. The pair density $\tilde{\rho}_n(r)$ has comparable or larger magnitude $\tilde{\rho}_n(r) \gtrsim \rho_n(r)$ with the normal density $\rho_n(r)$ in the skin region $r \sim R_{\rm surf} + 2$ fm and far outside. As discussed in Ref. [37], the exponential tail constant of the neutron pair density $\tilde{\rho}_n(r)$ in the asymptotic external region is related to the Fermi energy. The asymptotic tail develops as the drip line is approached and is longer than that of the normal density $\rho_n(r)$. Consequently, the di-neutron correlation in the external low-density region becomes relatively stronger in nuclei near the neutron drip line.

### C. Di-neutron correlation and single-particle configurations

In obtaining the significant di-neutron correlation, it is essential to adopt a large model space of neutron quasiparticle states including continuum orbits up to large quasiparticle energy ($E_{\rm max} = 50$ MeV in the present calculation) and large orbital angular momentum ($l_{\rm max} = 12$). If the oxygen isotopes, for example, are chosen, one would consider that neutron single-particle orbits $2s_{1/2}$ and $1d_{5/2,3/2}$ lying around the neutron Fermi energy are those most responsible for the neutron pairing. (Note that the Woods-Saxon $1d_{3/2}$ orbit is not a bound orbit but a resonance close to the zero energy. See Fig. 1.) However, if one truncates to a single-$j$ orbit or to orbits in one major shell, the di-neutron correlation never shows up: The two-body correlation density would exhibit a mirror symmetry with respect to the $x$-$y$ plane if only orbits with the same parity are taken into account. Importance of configuration mixing involving single-particle orbits in a large space as well as mixing with different parities and orbital angular momenta has been pointed out for the spatial localization of the correlated two-valence neutrons around a closed-shell core [19–22]. In the case of $2n$-halo nucleus $^{11}$Li, mixing with $s$ and $p$ orbits is suggested to cause the localization [17]. A similar but qualitative argument on the superconducting BCS wave function is also given in Ref. [70]. Here we shall clarify from a similar viewpoint the nature of configuration mixing responsible for the di-neutron correlation observed in the HFB description of the medium mass neutron-rich nuclei, where more than two weakly bound nucleons participate in the pair correlation.

In Fig. 7, we show partial contributions of neutron quasiparticle orbits truncated with respect to the orbital angular momentum $l$ of the orbits. Namely, the two-body correlation density is evaluated by including the neutron quasiparticle states obtained in the HFB calculation only up to a cutoff orbital angular momentum $l_{\rm cut}$. By including both parities but with low angular momenta $l = 0, 1, 2$ (covering at least all the neutron bound Woods-Saxon single-particle orbits in $^{22}$O), the spatial correlation at the internal position is rather well reproduced, but it is insufficient to bring about

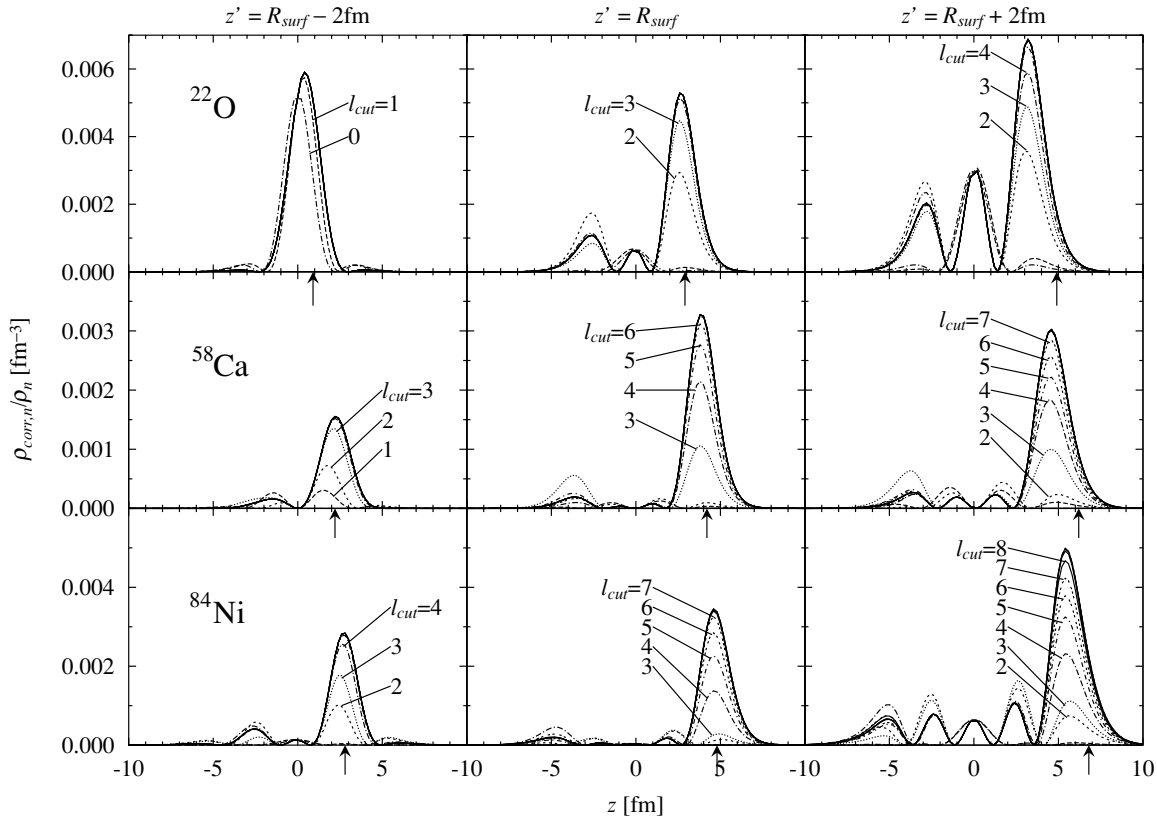


FIG. 7. Dependence of the neutron two-body correlation density on the orbital angular momentum cutoff $l_{\rm cut} = 0, 1, 2, 3, \cdots$ for $^{22}$O, $^{58}$Ca, and $^{84}$Ni in the top, middle, and bottom rows, respectively. Two-body correlation density is plotted along the $z$ axis. Full result is drawn with the solid line. Reference neutron positions fixed at the internal ($z' = R_{\rm surf} - 2$ fm), surface ($z' = R_{\rm surf}$), and external ($z' = R_{\rm surf} + 2$ fm) positions are shown by arrows in the left, middle, and right columns, respectively.

the correlation at the surface and the external positions; see the line corresponding to $l_{\rm cut} = 2$. Adding $l = 3$ orbits, the di-neutron correlation becomes more visible, but at the external position an approximate convergence is achieved only by including further $l = 4-5$ orbits. It should be noted here that the neutron quasiparticle orbits with high angular momentum ($l > 2$) are continuum states with $E > |\lambda_n|$. Figure 7 indicates that the continuum high-$l$ orbits are important at the surface and external positions also in Ca and Ni isotopes, for which a larger value of angular momenta up to $l \sim 6-8$ at $z' = R_{\rm surf}$ and $l \sim 7-9$ at $z' = R_{\rm surf} + 2$ fm are necessary. The above result pointing to the configuration mixing with different parities and orbital angular momenta goes along the line of the previous studies [17,19,21,22]. Note that significant high-$l$ orbits are involved to form the di-neutron correlation as the reference position moves far outside the surface.

The large contribution of the neutron high-$l$ quasiparticle orbits in the skin region can be related to the fact that the spatial correlation is enhanced at small distances $|\boldsymbol{r} - \boldsymbol{r}'| < 2-3$ fm. To illustrate we consider a pair of neutrons correlated in the *relative s-wave* at zero relative distance and whose center of gravity is located off the nuclear center. A corresponding two-particle wave function is written as $\sim\delta(\boldsymbol{r} - \boldsymbol{r}') \propto \sum_{lm}^{\infty} Y_{lm}^*(\boldsymbol{r}) Y_{lm}(\boldsymbol{r}')$ where $l$ is the orbital angular momentum about the nuclear center. This expression indicates that a coherent superposition of orbits with all orbital angular momenta $l$ are necessary for such a correlation. On a similar basis, we can argue that a superposition of angular momenta up to $l_M$ is needed to describe the di-neutron correlation which is dominantly in the relative $s$-wave and has a width approximately given by $\xi_d \sim 2r/l_M$ with respect to the angular direction ($r$ being the radial position of the center of gravity of the pair, and $\xi_d$ is the length scale of the di-neutron correlation). If we use $\xi_d \sim 2$ fm, the above estimate gives a qualitative (though not precise) account of the maximum angular momentum seen in Fig. 7.

We have also examined the contribution of high-lying neutron quasiparticle orbits. For this analysis, we reperform HFB calculations using smaller values of the cutoff energy $E_{\rm max}$ for the quasiparticle states, and we look into dependence on $E_{\rm max}$. To remove trivial effects originating from a reduction of the pairing correlation, we readjust the pairing force parameter $V_0$ to keep the same average pairing gap: $\langle\Delta_n\rangle = 1.52$, 1.27, and 1.35 MeV for $^{22}$O, $^{58}$Ca, and $^{84}$Ni. Results obtained with different values of $E_{\rm max}$ are shown in Fig. 8. Here we plot the probability of the pair wave function $p_n(\boldsymbol{r}\uparrow, \boldsymbol{r}'\downarrow) = \tilde{\rho}_n(\boldsymbol{r}\sigma, \boldsymbol{r}'\tilde{\sigma}')^2$ in place of the correlation density $\rho_{{\rm corr},n}(\boldsymbol{r}\uparrow, \boldsymbol{r}'\downarrow) = p_n(\boldsymbol{r}\uparrow, \boldsymbol{r}'\downarrow) - \rho_n(\boldsymbol{r}\uparrow, \boldsymbol{r}'\downarrow)^2$ in order to focus on the effect on the pair wave function. (The comparison between the solid lines in Fig. 7 and those in Fig. 8 shows that the second term in the above equation is negligible.)

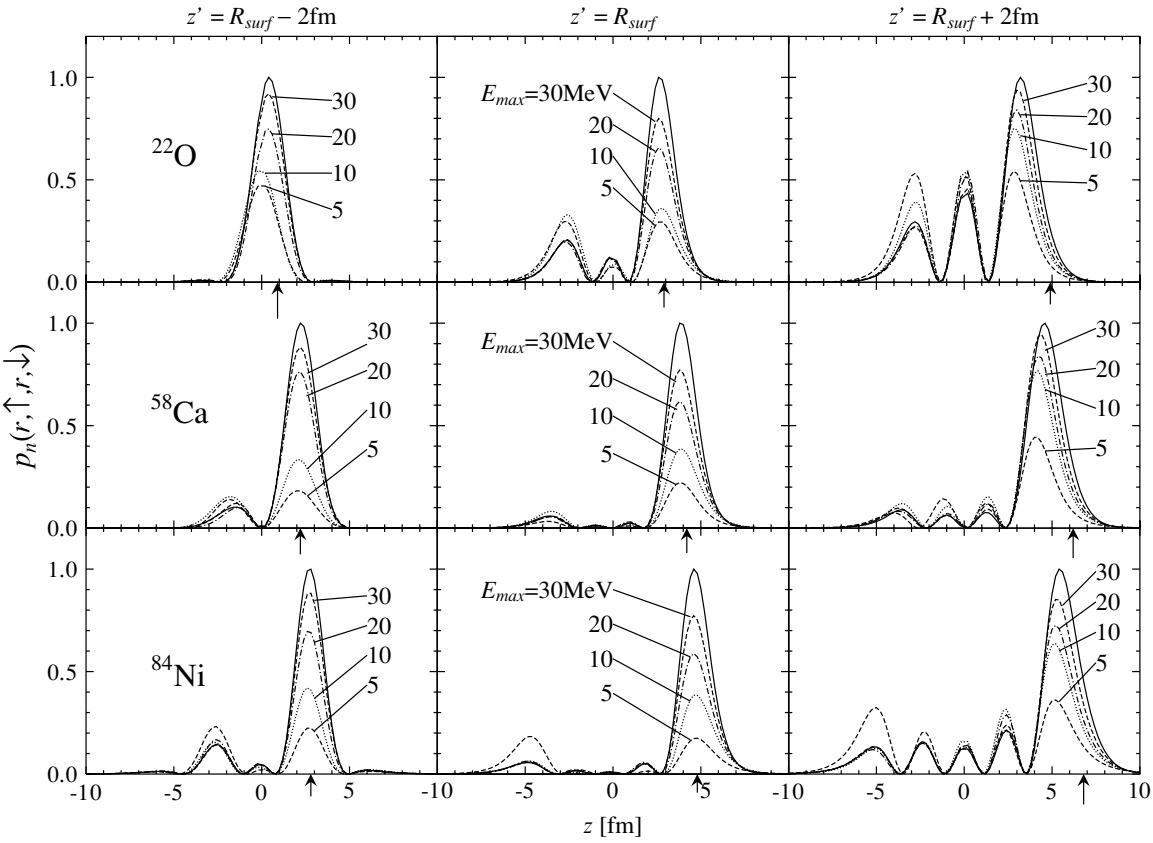


FIG. 8. Dependence of the neutron two-body correlation density on the quasiparticle energy cutoff $E_{\max}$. Here we evaluate only the second last term $p_n(\boldsymbol{r}\sigma, \boldsymbol{r}'\sigma') = \tilde{\rho}_n(\boldsymbol{r}\sigma, \boldsymbol{r}'\tilde{\sigma}')^2$ in Eq. (7) for different values of $E_{\max} = 5$, 10, 20, 30, 50 MeV, and we plot it by using a scale relative to the $E_{\max} = 50$ MeV result (solid line). Rows and columns correspond to the nuclides and the reference positions, respectively, as in Fig. 7. See also the text.

As indicated in Fig. 8, the di-neutron correlation barely appears if we use the small space including only up to $E_{\max} = 5$ MeV, which usually covers most of the quasiparticle states in one major shell. The results with $E_{\max} = 10, 20$ MeV display only weak di-neutron correlation, and one needs neutron quasiparticle states at least up to $E \sim 30$ MeV to obtain a qualitative account of the di-neutron correlation.

The above analysis also indicates a important role of continuum quasiparticle states for the di-neutron correlation. As the neutron Fermi energy is small ($-\lambda_n = 3.54$, 2.13, and 0.72 MeV in the case of $^{22}$O, $^{58}$Ca, and $^{84}$Ni, respectively), the quasiparticle states that contribute to the di-neutron correlation are mostly those embedded in the continuum energy region $E > |\lambda_n|$. Most of the neutron continuum states are non resonant states except for a few corresponding to the hole neutron orbits (e.g., $1p_{1/2,3/2}$ and $1s_{1/2}$) which have specific quasiparticle energies. The slow convergence with respect to the quasiparticle energy indicates that the nonresonant continuum states give nonnegligible and accumulating contributions to the di-neutron correlation. It is noted that the contribution of quasiparticle states with relatively small quasiparticle energy is important in the case of the external position. This may be related to the fact that the pair correlation becomes weaker in the external region.

### D. Dependence on pair interaction and particle-hole mean field

It is expected that the density dependence of the pairing interaction influences the di-neutron correlation since the pairing forces of the surface and the mixed types give stronger neutron-neutron attraction in the surface and the external regions than in the interior. The volume pairing force (the density-independent force) does not have this feature. To examine the influence of density dependence, we perform calculations using the surface and volume pairing forces. The pairing force strength $V_0$ chosen to reproduce the same average pairing gap $\langle\Delta_n\rangle$ calculated with the mixed pairing force. The calculated two-body correlation density shown in Fig. 9 indicates that the density dependence indeed affects the di-neutron correlation. Namely, in the case of surface pairing, the calculated two-body correlation density is significantly large in the surface (e.g., $z' = R_{\rm surf}$) and the exterior regions ($z' = R_{\rm surf} + 2$ fm) but it is weak in the internal region ($z' = R_{\rm surf} - 2$ fm). The volume pairing force does not exhibit such a position dependence. In the case of the mixed pairing force, the two-body correlation displays an intermediate feature as seen from comparison of Figs. 7 and 9.

We emphasize also that the di-neutron correlation cannot be properly described if one adopts the schematic seniority

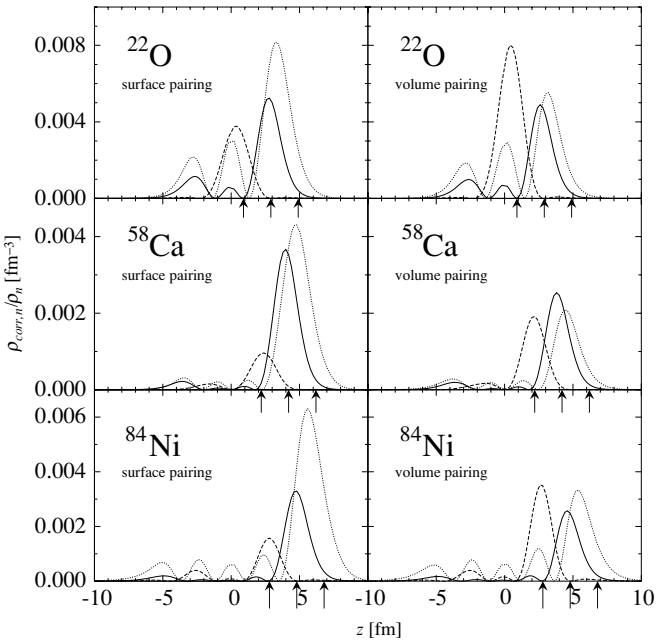


FIG. 9. Neutron two-body correlation density along the $z$ axis in $^{22}$O, $^{58}$Ca, and $^{84}$Ni calculated with the surface and the volume pairing forces having different density dependence. Dashed, solid, and dotted lines in each panel display this quantity for the internal, surface, and external positions of reference neutron. The pairing force parameters are $V_0 = -375, -395, -385$ MeV fm$^3$ (in $^{22}$O, $^{58}$Ca, and $^{84}$Ni, respectively) and $\rho_0 = 0.19$ fm$^{-3}$ for the surface pairing, and $V_0 = -190, -178, -180$ MeV fm$^3$ ($^{22}$O, $^{58}$Ca,$^{84}$Ni) for the volume pairing.

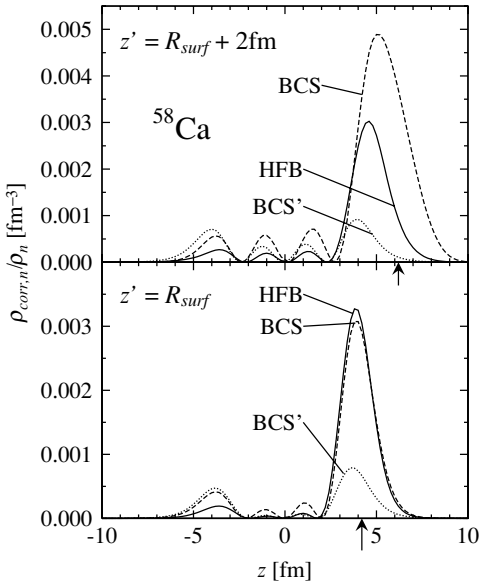


FIG. 10. Neutron two-body correlation density along the $z$ axis in the BCS approximation for $^{58}$Ca with use of a constant pairing gap $\Delta_n = 1.27$ MeV (dashed line). The HFB result (solid line) is shown for comparison. Another BCS result using only the bound Woods-Saxon neutron orbits is also shown by the dotted line (labeled BCS′). The reference neutron is placed at the external position $z' = R_{\rm surf} + 2$ fm in the upper panel; it is at the surface $z' = R_{\rm surf}$ in the lower panel.

pairing force used together with the conventional BCS approximation, where a constant pairing gap $\Delta_0$ is assumed instead of the self-consistent pair potential $\Delta(\boldsymbol{r})$. This is illustrated in Fig. 10, where we present a BCS calculation obtained with use of the standard analytic expression of $u, v$ factors, the Woods-Saxon single-particle energies, and the gap constant $\Delta_0$. We include all bound and discretized continuum Woods-Saxon neutron orbits (obtained with the box radius $r_{\rm max} = 20$ fm) and use the same cutoff parameters $E_{\rm max} = 50$ MeV and $l_{\rm max} = 12$ as in the HFB calculation. The value of $\Delta_0$ is set to that of the average neutron gap $\langle\Delta_n\rangle$ obtained in the HFB calculation. It is seen that the BCS calculation significantly overestimates the correlation density when the reference neutron is placed at external positions. In the case of surface and internal positions, the disagreement with the HFB is less serious, but profiles of the two-body correlation density are not well reproduced, as shown in Fig. 10. The unwanted overestimate in the external region arises from contributions of the discretized Woods-Saxon orbits in the positive-energy continuum region, for which the BCS approximation is known to cause unphysical correlation [37]. If we neglect the discretized continuum Woods-Saxon orbits to avoid this difficulty, however, the BCS approximation produces a result (dotted line in Fig. 10) that is far off the HFB result, and the di-neutron correlation never shows up.

We also examined whether the pairing properties depend on our choice of the Woods-Saxon model for the particle-hole mean field $h_q$. For this purpose, we performed a fully self-consistent HFB calculation that adopts the Skyrme force to derive the particle-hole mean field. Numerical procedures are the same as described in Sec. II A except that the Skyrme Hartree-Fock mean-field Hamiltonian with the SLy4 parameter set [71] is used for $h_q$. The Hartree-Fock neutron single-particle states are located slightly more deeply than the Woods-Saxon states and have larger single-particle level spacing due to the smaller effective mass: The energies of the last bound orbits are, for example, $e_{1d_{5/2},2s_{1/2},1d_{3/2}} = -6.58, -4.60, -0.64$ MeV in $^{22}$O, and $e_{1f_{7/2},2p_{3/2},2p_{1/2},1f_{5/2}} = -10.46, -6.61, -4.57, -3.45$ MeV in $^{58}$Ca, while the corresponding Woods-Saxon states have $e_{1d_{5/2},2s_{1/2}} = -4.94, -3.44$ MeV and $e_{1f_{7/2},2p_{3/2},2p_{1/2},1f_{5/2}} = -7.75, -4.81, -3.28, -2.53$ MeV (see also Fig. 1). We readjust the strength $V_0$ of the mixed pairing interaction so as to reproduce the same average gap. A representative result calculated for $^{58}$Ca is shown in Fig. 11, where comparison with the Woods-Saxon calculation is also made. Note that the value $V_0 = -310$ MeV fm$^3$ adopted for the Hartree-Fock is larger than the $V_0 = -280$ MeV fm$^3$ used for the Woods-Saxon case, reflecting the larger level spacings. It is seen in Fig. 11 that two-body correlation density $\rho_{{\rm corr},n}(\boldsymbol{r}\uparrow, \boldsymbol{r}'\downarrow)$ calculated with the Skyrme HFB exhibits the di-neutron correlation, i.e., the enhanced distribution at short relative distances $|\boldsymbol{r} - \boldsymbol{r}'| \lesssim 2-3$ fm, which is quite similar to those obtained with the Woods-Saxon potential.

### E. Di-neutron correlation and coherence length

It is interesting to compare the di-neutron correlation observed in the two-body correlation density in our HFB

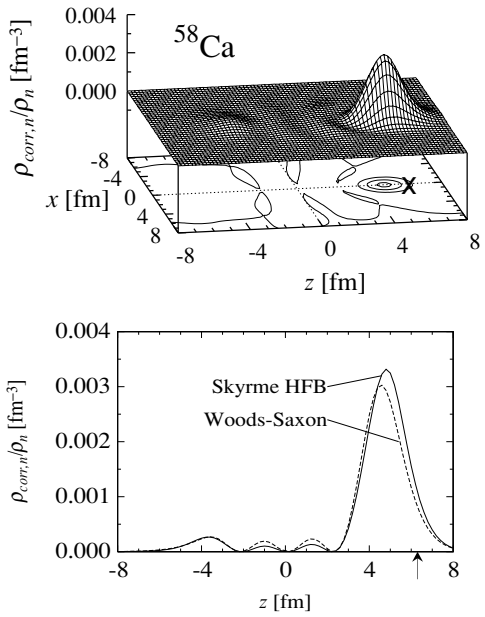


FIG. 11. (Top) Neutron two-body correlation density for $^{58}$Ca plotted on the $x$-$z$ plane in the Skyrme HFB calculation with the SLy4 parameter set. The reference neutron is placed at the external position $z' = R_{\rm surf} + 2$ fm, where the half-density radius is $R_{\rm surf} = 4.3$ fm. The adopted pairing force strength $V_0 = -310\,{\rm MeV\,fm}^3$ gives the same average pairing gap $\langle\Delta_n\rangle = 1.28$ MeV as that obtained with the Woods-Saxon model. (Bottom) Same quantity is plotted along the $z$ axis (solid line). Arrow indicates positions $z' = R_{\rm surf} + 2$ fm. For comparison, with the result obtained with the Woods-Saxon model (corresponding to the middle right panel in Fig. 3), is shown (dashed line).

calculation with the characteristics of the pair wave function known in the BCS theory of superconducting uniform matter. In the standard BCS description, the pair wave function $\psi_{\rm pair}(\boldsymbol{r}\sigma, \boldsymbol{r}'\sigma') \propto \tilde{\rho}_n(\boldsymbol{r}\sigma, \boldsymbol{r}'\tilde{\sigma}')$ exhibits a relative $s$ wave proportional to $\sin(k_F r_{12})/r_{12}$ ($r_{12} = |\boldsymbol{r} - \boldsymbol{r}'|$) multiplied with a radial function which damps asymptotically as $\sim e^{-r_{12}/\pi\xi_P}/\sqrt{r_{12}}$ for large $r_{12}$, where $\xi_P = \hbar v_F/\pi\Delta$ is the Pippard's coherence length, and $k_F(v_F)$ and $\Delta$ are the Fermi momentum (velocity) and the pairing gap, respectively [72]. The coherence length represents the size of the pair wave function. If we use typical values of $k_F \sim 1.4$ fm$^{-1}$ and $\Delta \sim 1$ MeV, an estimate based on the above expression gives $\xi_P \sim 20$ fm, which is much larger than the nuclear radius [73], implying broad spreading of the pair wave function in the whole region of nuclear volume. The correlation density $\rho_{{\rm corr},n}(\boldsymbol{r}\sigma, \boldsymbol{r}'\sigma') \sim \tilde{\rho}_n(\boldsymbol{r}\sigma, \boldsymbol{r}'\tilde{\sigma}')^2$ calculated in the present HFB calculation appears to display a feature of the relative $s$ wave for $r_{12}$ less than a few fm, and the first node around $r_{12} \sim 2$ fm could be related in the case of the internal positions to the oscillation period $\pi/k_F \sim 2$ fm suggested in the BCS pair wave function. (We here follow the discussion in Ref. [22], where a behavior similar to $\sin(k_F r_{12})/r_{12}$ was previously pointed out in the case of the correlated two-valence neutrons in $^{210}$Pb.) On the other hand, the localization with the large probability $\sim$30$-$60% in the short distance region $r_{12} \lesssim$ 2–3 fm observed in the HFB calculation appears much stronger than what is expected from the simple coherence length estimate.

We note that the two-neutron correlation in the HFB description of the neutron pairing is calculated also by Barranco *et al*. [74] for the nonuniform low-density neutron matter in a Wigner-Seiz cell with an immersed lattice "nucleus," approximating the situation of an inner crust of neutron stars. The authors point out that the root-mean-square relative distance weighted with the two-neutron probability density coincides approximately with Pippard's coherence length $\xi_P$. The calculated two-neutron probability itself (Fig. 3 in Ref. [74]), on the other hand, shows a distribution that forms a sharp and large peak at short relative distances $|\boldsymbol{r} - \boldsymbol{r}'| \lesssim 2$ fm, indicating a behavior similar to the di-neutron correlation discussed in the present investigation. The HFB calculation in Ref. [74] adopts the finite range Gogny force [75] as the effective pairing force. Combining the results of Ref. [74] and ours, it can be suggested also that the qualitative feature of the di-neutron correlation persists irrespective of detailed forms of the effective pairing force. The quantitative aspects, however, will depend on the effective interaction, as we already discussed in the previous subsection.

## III. DI-NEUTRON CORRELATION IN THE SOFT DIPOLE EXCITATION

### A. Continuum QRPA description of the soft dipole excitation

We first recapitulate briefly the continuum QRPA method [48], which we adopt to describe the dipole excitation of nuclei near the drip line. It provides a fully microscopic description of a linear response of the nucleus excited by an external perturbing field by taking into account all nucleon degrees of freedom. It is formulated as the small amplitude limit of a time-dependent extension (TDHFB) of the coordinate-space HFB theory, which we utilize for the description of the ground state. Consequently, the description is constructed in a self-consistent manner. The linear responses in the normal and the pair densities are the basic quantities of the description. They are governed by the RPA density response equation called also the Bethe-Salpeter equation [44]:

$$\begin{pmatrix} \delta\rho_{qL}(r,\omega) \\ \delta\tilde{\rho}_{+,qL}(r,\omega) \\ \delta\tilde{\rho}_{-,qL}(r,\omega) \end{pmatrix} = \int_0 dr' \big[R^{\alpha\beta}_{0,qL}(r,r',\omega)\big] \begin{pmatrix} \sum_{q'} \kappa^{qq'}_{\rm ph}(r')\delta\rho_{q'L}(r',\omega)/r'^2 + v^{\rm ext}_{qL}(r') \\ \kappa_{\rm pair}(r')\delta\tilde{\rho}_{+,qL}(r',\omega)/r'^2 \\ -\kappa_{\rm pair}(r')\delta\tilde{\rho}_{-,qL}(r',\omega)/r'^2 \end{pmatrix}. \quad (9)$$

Here, the excitation with multipolarity $L$ and frequency $\omega$, and use of contact forces are assumed. The functions $\kappa_{\rm ph}(r)$ and $\kappa_{\rm pair}(r)$ represent the residual interaction associated with the density variations. An important feature of the present response equation is that we include the particle-particle channel, i.e., the second and third rows in Eq. (9) containing $\delta\tilde{\rho}_{+,qL}(r',\omega)$ and $\delta\tilde{\rho}_{-,qL}(r',\omega)$, which correspond to the variations in the pair densities $\delta\tilde{\rho}_{\pm,q}(\boldsymbol{r}t) = \delta\langle\Phi(t)|\frac{1}{2}\sum_\sigma[\psi_q^\dagger(\boldsymbol{r}\sigma)\psi_q^\dagger(\boldsymbol{r}\tilde{\sigma}) \pm \psi_q(\boldsymbol{r}\tilde{\sigma})\psi_q(\boldsymbol{r}\sigma)]|\Phi(t)\rangle$ as well as the one in the normal density $\delta\rho_q(\boldsymbol{r}t) = \delta\langle\Phi(t)|\sum_\sigma \psi^\dagger(\boldsymbol{r}\sigma)\psi(\boldsymbol{r})|\Phi(t)\rangle$ in the particle-hole channel, represented by the first row. To derive Eq. (9), a linear perturbation in the time-evolving TDHFB state vector $|\Phi(t)\rangle$ is considered. The products $\kappa_{\rm pair}(r)\frac{1}{r^2}\delta\tilde{\rho}_{\pm,qL}(r,\omega)$ of the residual interaction $\kappa_{\rm pair}(r)$ and the pair density variations represent the dynamical change $\delta\Delta(\boldsymbol{r}t)$ of the pair potential associated with the time evolution. The two-point function $R^{\alpha\beta}_{0,qL}(r,r',\omega)$ is the unperturbed response function for the three kinds of densities $\delta\rho(r)$ and $\delta\tilde{\rho}_\pm(r)$, which are indexed by $\alpha$ and $\beta$. Through the recursive relation for the density responses in Eq. (9), the RPA correlations with infinite orders of the residual interactions are taken into account. The RPA correlation acting in the particle-particle channel, which is associated with the residual pair interaction $\kappa_{\rm pair}$, may be called the *dynamical pair correlation* [31,32,48]. As the external field, whose radial form factor is represented by $v^{\rm ext}_{qL}(r)$, we consider the dipole operator

$$D_\mu = e\frac{Z}{A}\sum_{i\in n}(rY_{1\mu})(\boldsymbol{r}_i) - e\frac{N}{A}\sum_{i\in p}(rY_{1\mu})(\boldsymbol{r}_i), \tag{10}$$

in which the spurious center of mass motion is explicitly removed. As the effective nuclear force, we adopt the density-dependent delta forces. We employ the same pairing force $v_{\rm pair}$ used in the description of the ground state to derive the particle-particle residual interaction $\kappa_{\rm pair}$. Thus the self-consistency is achieved in treating correlations in the particle-particle channel. As the effective force responsible for the particle-hole correlation, we adopt a delta interaction of the Skyrme type [55]:

$$v_{\rm ph}(\boldsymbol{r},\boldsymbol{r}') = [t_0(1+x_0P_\sigma) + t_3(1+x_3P_\sigma)\rho(\boldsymbol{r})]\,\delta(\boldsymbol{r}-\boldsymbol{r}'). \tag{11}$$

As the particle-hole mean field (the Woods-Saxon potential) and the particle-hole residual interaction are not derived from a common effective interaction, the two are not self-consistent. We, therefore, impose according to Ref. [55] an approximate self-consistency in the particle-hole channel by renormalizing the force strengths as $t_{0,3} \to f t_{0,3}$ so that the lowest energy dipole mode corresponding to the spurious center of mass motion has the zero excitation energy. As this procedure gives a reasonable description of particle-hole correlation in the giant resonances in closed-shell stable nuclei [55], we expect the same for the soft dipole excitation, for which correlation caused by the particle-hole residual interaction is suggested to be rather weak [25–27]. With this choice, the residual interaction reads

$$\kappa_{\rm ph}^{q=q'}(r) = \frac{t_0}{2}(1-x_0) + \frac{t_3}{12}[(5+x_3)\rho(r) - (2+4x_3)\rho_q(r)], \tag{12}$$

$$\kappa_{\rm ph}^{q\neq q'}(r) = t_0\left(1+\frac{x_0}{2}\right) + \frac{t_3}{12}(5+x_3)\rho(r), \tag{13}$$

$$\kappa_{\rm pair}(r) = \frac{V_0}{2}\left[1-\frac{\rho(r)}{\rho_0}\right]. \tag{14}$$

In the present continuum QRPA method, special attention is paid to treatment of the continuum states that play essential roles for excitations embedded in the energy region above the threshold of nucleon escaping. To this end, we evaluate the unperturbed response functions $R^{\alpha\beta}_{0,qL}$ by means of an integral representation that uses a contour integral in the complex quasiparticle energy plane [48]:

$$\begin{aligned} R^{\alpha\beta}_{0,qL}(r,r',\omega) = \frac{1}{4\pi i}\int_C dE \sum_{lj,l'j'}\frac{\langle l'j'\|Y_L\|lj\rangle^2}{2L+1} \\ \times [\mathrm{Tr}\,\mathcal{A}_\alpha\mathcal{G}_{0,ql'j'}(r,r',E+\hbar\omega+i\epsilon) \\ \times \mathcal{B}_\beta\mathcal{G}_{0,qlj}(r',r,E) + \mathrm{Tr}\,\mathcal{A}_\alpha\mathcal{G}_{0,qlj}(r,r',E) \\ \times \mathcal{B}_\beta\mathcal{G}_{0,ql'j'}(r',r,E-\hbar\omega-i\epsilon)]. \end{aligned} \tag{15}$$

Here $\mathcal{G}_{0,qlj}(E) = (E-\mathcal{H}_{0,qlj})^{-1}$ is the HFB Green function in the partial wave $lj$, which describes propagation of nucleons under influence of the pair potential $\Delta(r)$ and the particle-hole mean field (the Woods-Saxon potential). We use the exact form of the HFB Green function $\mathcal{G}_{0,qlj}(E)$ [76], which is given as a product of the regular and outgoing solutions of the HFB equation (2) so that $\mathcal{G}_{0,qlj}(E)$ satisfies the outgoing boundary condition appropriate for continuum quasiparticle states. The combined use of the integral representation Eq. (15) and the exact HFB Green function is the key ingredient of the present continuum QRPA method. Note that the present scheme takes precise account of two quasiparticle configurations where two nucleons occupy simultaneously continuum orbits since the two quasiparticles are both described by the outgoing HFB Green function in Eq. (15). Furthermore, the particle-particle and the particle-hole correlations acting among such two-quasiparticle configurations are included through the density response equation (9). The energy-weighted sum rule (the TRK sum rule) is satisfied within about 1% thanks to the self-consistent treatment of the pair correlations and the use of the exact HFB Green function. Detailed derivation and other aspects of the continuum QRPA method are discussed in Ref. [48].

Some physical quantities are calculated directly from the solution of the density response equation. The $E1$ strength function for the dipole excitation is given by $S_{E1}(E=\hbar\omega) = dB(E1)/dE = -\frac{3}{\pi}\mathrm{Im}\sum_q\int dr\, v^{\rm ext}_{qE1}(r)^*\delta\rho_{qL=1}(r,\omega)$. We can also characterize the excitation mode by means of the transition densities. The particle-hole transition density for an excited state $|\Phi_i\rangle$, at the excitation energy $E_i$ (i.e., with the frequency $\omega_i = E_i/\hbar$) is given by

$$\rho^{\rm ph}_{iq}(\boldsymbol{r}) = \langle\Phi_i|\sum_\sigma\psi_q^\dagger(\boldsymbol{r}\sigma)\psi_q(\boldsymbol{r}\sigma)|\Phi_0\rangle = Y^*_{LM}(\hat{\boldsymbol{r}})\rho^{\rm ph}_{iqL}(r), \tag{16}$$

$$\rho^{\rm ph}_{iqL}(r) = -\frac{C}{\pi r^2}\,\mathrm{Im}\,\delta\rho_{qL}(r,\omega_i), \tag{17}$$

with use of the density response $\delta\rho_{qL}(r,\omega)$ in the particle-hole channel. We normalize the transition density by a constant $C$

so that the transition amplitude for the $E1$ operator, $M_{iq} = \int dr r^2 v_q^{\rm ext}(r)\rho_{iqL}^{\rm ph}(r)$, gives the $E1$ strength $B(E1, 0^+_{\rm g.s.} \to 1^-_i) = \int_{E_1}^{E_2} S_{E1}(E)dE = 3M_{iq}^2$ integrated over a certain energy interval around the excitation energy $E = \hbar\omega_i$ of the state under consideration.

The present continuum QRPA also enables us to evaluate two kinds of transition amplitudes for pairs of nucleons:

$$P_{iq}^{\rm pp}(\boldsymbol{r}) = \langle \Phi_i | \psi_q^\dagger(\boldsymbol{r}\uparrow)\psi_q^\dagger(\boldsymbol{r}\downarrow)|\Phi_0\rangle = Y_{LM}^*(\hat{\boldsymbol{r}})P_{iqL}^{\rm pp}(r), \quad (18)$$

$$P_{iq}^{\rm hh}(\boldsymbol{r}) = \langle \Phi_i | \psi_q(\boldsymbol{r}\downarrow)\psi_q(\boldsymbol{r}\uparrow)|\Phi_0\rangle = Y_{LM}^*(\hat{\boldsymbol{r}})P_{iqL}^{\rm hh}(r). \quad (19)$$

These pair transition densities provide information of how nucleon pairs move in the excited state. The first pair transition density $P_{iq}^{\rm pp}(\boldsymbol{r})$ can be related to an amplitude to produce the excited state by adding (or transferring) at the position $\boldsymbol{r}$ a spin-singlet nucleon pair with the relative $s$ wave to the ground state of the $A-2$ system. We call it the particle-particle or the particle-pair transition density hereafter. The second pair transition density $P_{iq}^{\rm hh}(\boldsymbol{r})$, which we call the hole-hole or the hole-pair transition density, on the other hand, is related to an amplitude of producing the excited state by removing a spin-singlet nucleon pair from the $A+2$ ground state. These pair transition densities are calculated as

$$P_{iqL}^{\rm pp}(r) = \frac{C}{2\pi r^2}\,{\rm Im}[\delta\tilde{\rho}_{+,qL}(r,\omega_i) - \delta\tilde{\rho}_{-,qL}(r,\omega_i)], \quad (20)$$

$$P_{iqL}^{\rm hh}(r) = \frac{C}{2\pi r^2}\,{\rm Im}[\delta\tilde{\rho}_{+,qL}(r,\omega_i) + \delta\tilde{\rho}_{-,qL}(r,\omega_i)], \quad (21)$$

with use of the pair density responses $\delta\tilde{\rho}_{\pm,qL}(r,\omega)$ obtained in the density response equation. Here the same normalization constant $C$ is adopted as for the particle-hole transition density.

The force parameters of the particle-hole residual interaction is chosen as $t_0 = -1100\,{\rm MeV\,fm^3}$, $t_3 = 16\,000\,{\rm MeV\,fm^6}$, $x_0 = 0.5$, and $x_3 = 1$ taken from Ref. [55]. The renormalization factor $f$ determined for each nucleus is $f = 0.708, 0.727, 0.750, 0.775$ for $^{18-24}$O; $f = 0.713, 0.735, 0.745$ for $^{50,54,58}$Ca; and $f = 0.735, 0.744, 0.749, 0.755$ for $^{80-86}$Ni. The same radial mesh as in solving the HFB equation (2) is used to solve Eq. (9). The maximum orbital angular momentum in the two-quasiparticle sum of Eq. (9) is $l_{\rm max} = 12$ in O and Ca isotopes, which is the same as in the HFB calculation for the ground state. In Ni isotopes we use a larger value $l_{\rm max} = 17$ and a larger radius cutoff $r_{\rm max} = 25$ fm to achieve better convergence in the continuum QRPA calculations. In this case, the HFB calculation is performed with the enlarged $l_{\rm max}$ and $r_{\rm max}$ although we do not see any sizable influence in the ground state properties. The same mixed pairing force as that in the HFB calculation is adopted as the reference choice. We adopt a small imaginary constant with $\epsilon = 0.2$ MeV, which corresponds to smoothing of the strength function convoluted with a Lorentzian with FWHM = 0.4 MeV. The calculated results shown below differ from those in the previous analysis [31], where calculations are done for $^{22}$O by using the surface-type pairing interaction ($\rho_0 = 0.16\,{\rm fm^{-3}}$) and a larger force strength $V_0 = -520\,{\rm MeV\,fm^3}$ adjusted to the conventional systematics of the pairing gap $\Delta_{\rm syst} = 12/\sqrt{A}$ MeV ($\sim$2.5$-$2.8MeV in the oxygen isotopes). Here the adopted value $V_0 = -280\,{\rm MeV\,fm^3}$ with $\rho_0 = 0.32\,{\rm fm^{-3}}$ is fixed so as to produce the odd-even mass difference ($\sim$0.5$-$2.0 MeV for the same isotopes), as discussed in Sec. II. Other numerical details are the same as in Ref. [31].

### B. $E1$ strength near neutron threshold energy

The $E1$ strength functions $S_{E1}(E) = dB(E1)/dE$ calculated for even-even isotopes $^{18-24}$O, $^{50,54,58}$Ca, and $^{80-86}$Ni near the drip line are presented in Fig. 12. In all nuclides the strength function exhibits significant distribution of the $E1$ strength just above the threshold energy $E_{\rm th,1} = \min(E_{\rm in}) + |\lambda_n|$ of one-neutron escaping and far below the giant dipole resonance energy ($E_{\rm GDR} \sim 20$ MeV in O and $\sim$15 MeV in Ni). This low-energy $E1$ strength increases significantly as the neutron drip line is approached. In many isotopes, the soft dipole excitation is situated also above the threshold energy $E_{\rm th,2} = 2|\lambda_n|$ of two-neutron escaping, which becomes low in nuclei near the drip line, especially in the nickel isotopes. The strength distribution in the giant dipole resonance region shows rather strong isotopic dependence in the case of the oxygen isotopes. The peak at the zero energy corresponds to the spurious center of mass motion, for which the energy-weighted strength is negligible. In the following, we concentrate on the soft dipole excitations.

The strength function in the region of the soft dipole excitation shows a smooth profile as a function of the excitation energy. It is not possible to evaluate the resonance width because the strength does not form a sharp resonance peak. The smooth profile implies that neutron escaping has a large influence on the soft dipole excitations. This is explicitly seen by comparing the profile with a calculation neglecting neutron escaping, shown in Fig. 13 for $^{22}$O. This calculation is done with use of the discretized continuum quasiparticle states obtained with the box boundary condition (the box radius $r_{\rm max} = 20$ fm), instead of using the exact Green function with the outgoing boundary condition adopted in the present continuum calculations. In the discretized calculation, there are several discrete peaks in the energy region of the soft dipole excitation. The four major peaks seen in the interval $E = 5-9$ MeV have different behaviors in the transition densities, while the transition densities in the continuum calculation vary smoothly as a function of the excitation energy. The soft dipole excitation cannot be represented by one of these discrete peaks.

The $E1$ strength in the soft dipole region is experimentally measured in neutron-rich oxygen isotopes, and the energy-weighted sum of the $E1$ strength below $E < 15$ MeV is extracted [9]. We evaluate the corresponding energy-weighted sum from the calculated strength function, as listed in Table II. The experimental value of the energy-weighted sum is about 8% of the Thomas-Reiche-Kuhn sum rule value in $^{18,22}$O and about 12% in $^{20}$O [9]. The calculation gives a fair agreement with the experimental data in $^{18,20}$O, but it overestimates in $^{22}$O. The agreement may be improved by refining the model Hamiltonian, e.g., the Woods-Saxon parameters, or by adopting a self-consistent Hartree-Fock

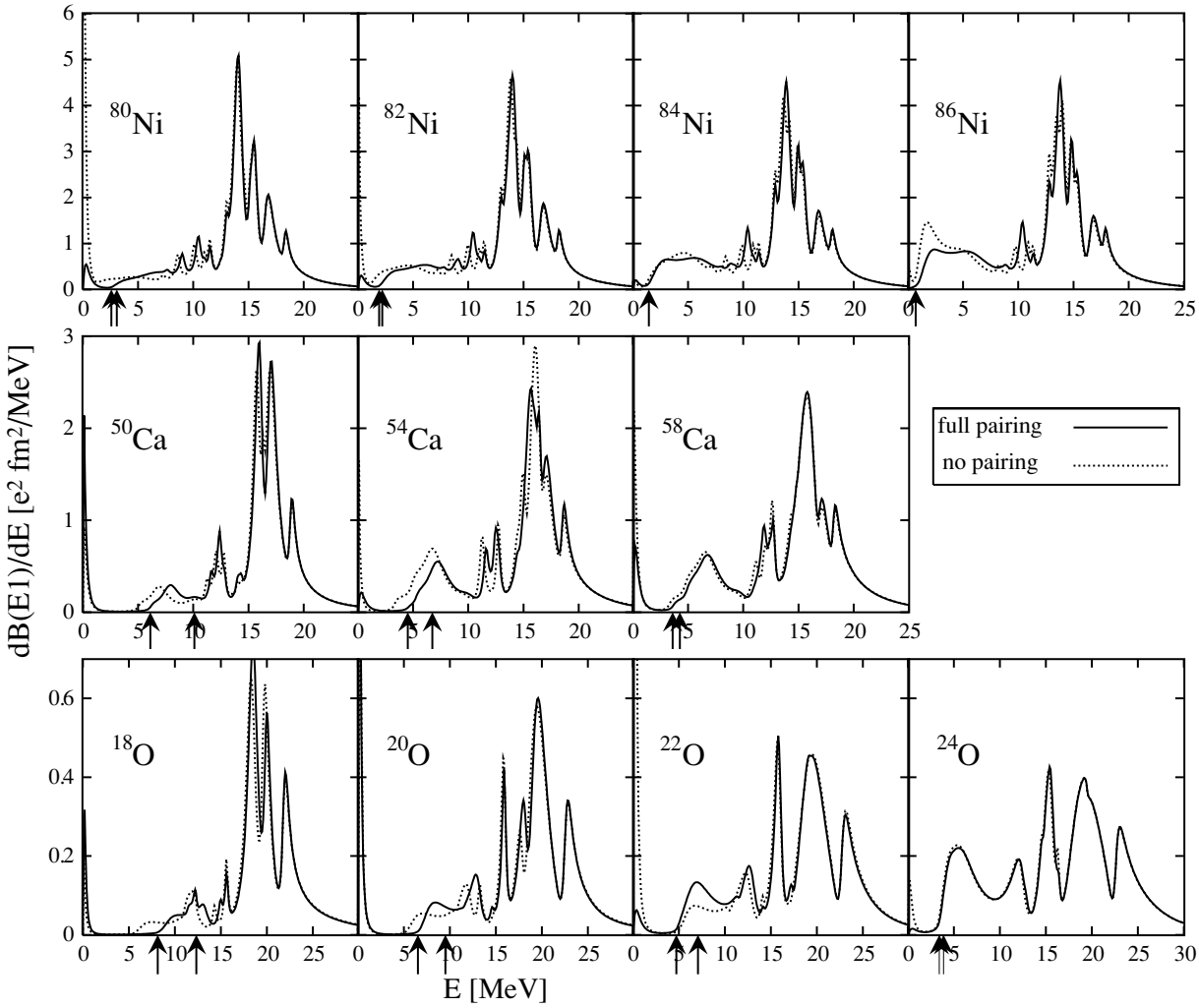


FIG. 12. $E1$ strength function in the neutron-rich even-even oxygen, calcium, and nickel isotopes near the drip line, calculated with the mixed pairing force (solid line). The result obtained without the pairing correlation (by use of a very weak pairing force $V_0 \approx 0$) is also plotted (dotted line). Renormalization constant $f$ is determined to achieve the approximate self-consistency for both cases with and without the pairing correlation. Arrows indicate the one- and the two- neutron threshold energies $E_{\mathrm{th},1}$ and $E_{\mathrm{th},2}$. Note that $E_{\mathrm{th},1} = E_{\mathrm{th},2}$ in $^{86}$Ni and $^{84}$Ni, where there are no bound quasiparticle states for neutrons.

potential which is expected to be more realistic. Note that the shell model [28] and the phonon coupling model [29] based on the Skyrme HF+BCS+QRPA approach exhibit a saturation around $^{22}$O.

Comparing among O, Ca, and Ni isotopic chains, we observe slightly different behaviors in the soft dipole excitation. In the case of Ni isotopes, the $E1$ strength is distributed at very low excitation energy as the neutron threshold energy is very low ($E_{\mathrm{th},1} \sim 0.70-2.45$ MeV). This can be related to the small neutron Fermi energy in the $A = 80-86$ nickel isotopes, which is only about $-1.50$ to $-0.40$ MeV. Note also that the single-particle energies of the most weakly bound neutron Woods-Saxon orbits $3s_{1/2}$ and $2d_{5/2}$ in the vicinity of the Fermi energy are small; $e_{3s_{1/2},2d_{5/2}} \sim -1$ MeV (Fig. 1). In Ca isotopes, the increase of the $E1$ strength above the neutron threshold energy $E_{\mathrm{th},1}$ is not as steep as in O and Ni, but a small peak is formed at the energy which slightly deviates from the threshold energy. This occurs because there is no weakly bound neutron $s$ orbit in the calcium isotopes, while $p$ orbits ($2p_{1/2,3/2}$) participate instead (see the following section for details).

### C. Pairing effects on dipole strength

We analyze effects of the neutron pair correlation on the soft dipole excitation, which is the primary issue in the present investigations. To visualize the influence of neutron pairing correlation, we perform a calculation where the neutron pairing interaction is switched off, i.e., by setting $V_0 = 0$. (For open subshell nuclei such as $^{18,20}$O, a very weak pairing interaction $V_0 = -28$ MeV fm$^3$ is used to guarantee a $J^\pi = 0^+$ configuration in the last $j$-shell orbit partially occupied in the ground state. This choice produces such a small average pairing gap $\langle \Delta_n \rangle < 0.1$ MeV that the pair correlation effects are negligible.) Calculated results are shown by the dotted line

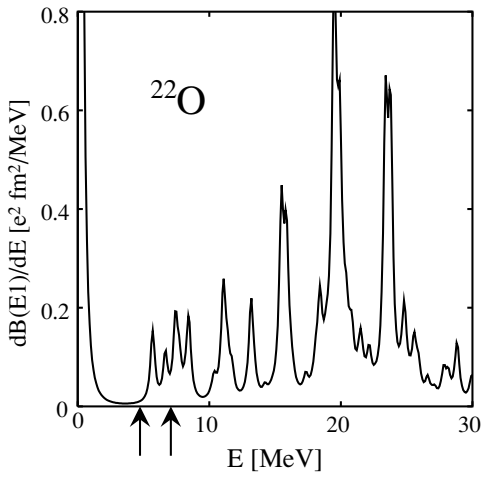


FIG. 13. $E1$ strength function in $^{22}$O, obtained by using the discretized continuum states and the box boundary condition, in the case of the mixed pairing force. See also the text.

in Fig. 12. We immediately see a sizable pairing effect on the $E1$ strength of the soft dipole excitation, whereas there is essentially no effect on the giant dipole resonance. To focus on the soft dipole excitation, we show a magnified portion of the dipole strength function in Fig. 14.

The effect of the neutron pairing correlation on the soft dipole strength varies depending on the isotopic chains and mass numbers.

(i) In the oxygen isotopes, the neutron pairing correlation significantly increases the $E1$ strength in the soft dipole region in $^{20,22}$O (and slightly less clearly in $^{18}$O). Table II lists the $B(E1)$ value of the soft dipole excitation integrated over an energy window of 4 MeV width above the one-neutron threshold energy $E_{\mathrm{th},1}$. The pairing correlation increases the $B(E1)$ value by about 50–80% in $^{18-22}$O. The energy-weighted sum of $B(E1)$ up to $E = 15$ MeV is also tabulated in Table II. The influence of pairing on the energy-weighted sum is relatively small compared with that on the $B(E1)$ value, because the pairing effect becomes weaker at higher excitation energies. The pairing effect is negligible in the case of $^{24}$O, but this is because the pair correlation itself is very small ($\langle\Delta_n\rangle = 0.66$ MeV) in this nucleus.

TABLE II. Calculated energy-weighted sum $S^1 = \int_0^E dE' E' \, dB(E1)/dE'$ of the $E1$ strength for the excitation energy below $E = 15$ MeV in the oxygen isotopes, and $B(E1) = \int_{E_1}^{E_2} dE' dB(E1)/dE'[e^2\ \mathrm{fm}^2]$ in an excitation energy interval of 4 MeV above the one-neutron threshold energy $E_{\mathrm{th},1}$. The value of $S^1$ is given as a fraction to the Thomas-Reiche-Kuhn sum rule value $S^1_{\mathrm{TRK}}$. We list also the results obtained without the neutron dynamical pairing correlation, and those neglecting all the neutron pairing correlations.

| | $^{18}$O | $^{20}$O | $^{22}$O | $^{24}$O |
|---|---|---|---|---|
| $S^1/S^1_{\mathrm{TRK}}$ ($E < 15$ MeV) | | | | |
| Full pairing | 6.8% | 10.2% | 13.6% | 19.4% |
| No pairing | 6.7% | 9.3% | 11.8% | 19.8% |
| $B(E1)$ [$e^2$ fm$^2$] ($E_{\mathrm{th},1} < E < E_{\mathrm{th},1} + 4$ MeV) | | | | |
| Full pairing | 0.188 | 0.254 | 0.393 | 0.702 |
| No dynamical pairing | 0.131 | 0.205 | 0.354 | 0.694 |
| No pairing | 0.104 | 0.175 | 0.235 | 0.718 |

(ii) In the calcium isotopes, the pairing correlation does not enhance the magnitude of $E1$ strength. Instead, it shifts the low-lying dipole strength up in the excitation energy and/or it suppresses the strength of the soft dipole excitation. The suppression in the $E1$ strength is about 20% in $^{54}$Ca (see Table III).

(iii) In the nickel isotopes, the neutron pair correlation either significantly suppresses the $E1$ strength at low energies (in $^{86}$Ni by about 30%, see Table III) or modifies the shape of the strength distribution (in $^{80-84}$Ni, see Fig. 14). After all, the pair correlation certainly influences the strength distribution of the soft dipole excitation, but it can either enhance (as in the case of $^{20,22}$O) or suppress (as in $^{54}$Ca,$^{86}$Ni) the $E1$ strength.

To analyze the pair correlation effect, it is useful to decompose it into the *static* and the *dynamical* mechanisms [31,48]. Note that the pair correlation causes the static pair potential $\Delta(\boldsymbol{r})$ in the HFB mean-field Hamiltonian. This mean-field effect modifies the ground state configuration and the single-particle excitation, through which the excitation properties are also affected. We call this mechanism *the static pair correlation effect*. On the other hand, the RPA correlation associated with the dynamical variation in the pair potential $\delta\Delta(\boldsymbol{r}\omega)$ gives the additional pair correlation effect on the excitation, which we call the *dynamical pair correlation effect*. In other words, the dynamical pair correlation effect originates from the residual interaction taken into account in the RPA equation (9), while the static effects are present even in the unperturbed response. To examine these pair correlation effects separately, we performed calculations where the dynamical pair correlation is neglected while keeping the static pairing effects. The result is shown in Fig. 14 with the dashed line. It is immediately seen that both the static and the dynamical correlations have considerable effect on the dipole strength in the soft excitation region.

Let us first focus on the static pairing effect. The static effect is a major part of the net pairing effect on the dipole strength and produces qualitative trends of the strength function, although the dynamical effect cannot be neglected for a quantitative description. To get more insight into the static effect, we look into the unperturbed strength function obtained by neglecting all the residual interactions for the RPA (Fig. 15). In the unperturbed strength, we separate contributions from different two-quasiparticle excitations by selecting a specified pair of angular momenta of the two-quasiparticle configurations. Taking $^{22}$O as an example, where the pairing effect on the soft dipole excitation is large, we find that the static pairing effect increases the unperturbed $E1$ strength. This arises mainly from a contribution of a neutron two-quasiparticle configuration exciting the $2s_{1/2}$ state and the continuum $p$ states coupled to $L = 1$, abbreviated as $[2s_{1/2} \times p^*]_{L=1}$ or more shortly $2s_{1/2} \times p^*$ (the asterisk denotes the continuum states), as seen by comparing between the left top and the left bottom panels of Fig. 15. This quasiparticle excitation is available

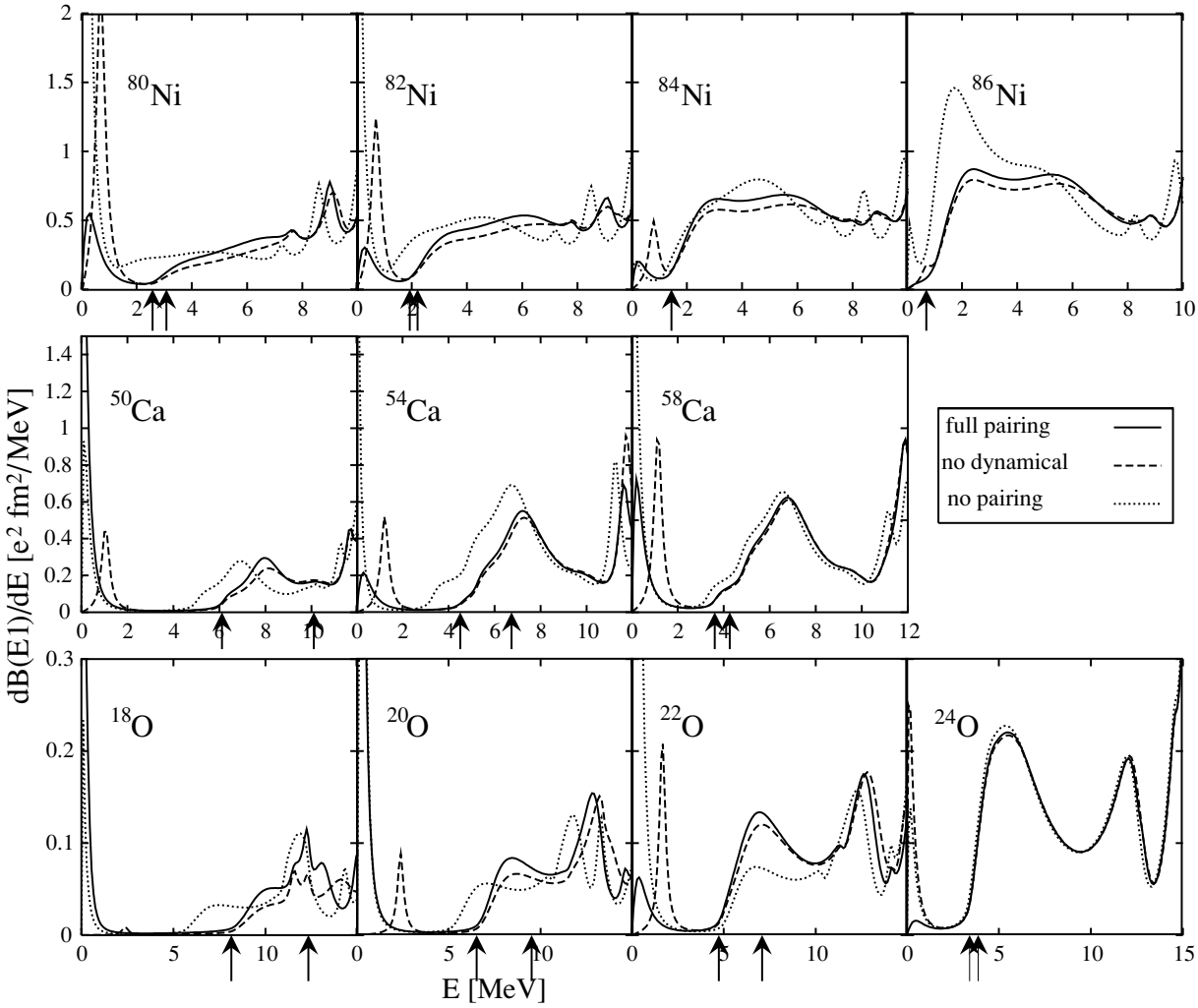


FIG. 14. Same as Fig. 12, but emphasizing the low excitation energy region and effects of the static and dynamical pairing correlations. For the latter purpose, the result obtained by neglecting the dynamical pairing correlation (while keeping the static pairing correlation) is plotted with the dashed line.

only by taking into account the ground state pair correlation, because the Woods-Saxon $2s_{1/2}$ orbit located above the Fermi energy (Fig. 1) can be partially occupied only if the pair correlation is included. The contribution of the $2s_{1/2} \times p^*$ configuration to the dipole strength is added with those of $1d_{5/2} \times p^*$ configurations, which are dominant ones when the pairing is neglected (see the lower panel of Fig. 15). In $^{18-20}$O, the increase of dipole strength due to the static pairing effect is similarly seen, but it is not very large since the occupation of the $2s_{1/2}$ orbit is smaller. Another aspect of the static pairing effect is that it pushes up the strength to a slightly higher energy. This happens because the pair correlation increases the energy of the two-quasiparticle excitation higher than that of the corresponding unpaired particle-hole excitation.

TABLE III. The calculated $E1$ strength $B(E1) = \int_{E_1}^{E_2} dE' dB(E1)/dE'$ ($e^2$ fm$^2$) of the soft dipole excitation in Ca and Ni isotopes. In Ca isotopes, the energy interval $[E_1, E_2]$ is chosen with $E_1 = 5.9, 5.2, 4.8$ MeV and $E_2 = E_1 + 4$ MeV to enclose the soft dipole peak in $A = 50, 54, 58$, respectively. In Ni isotopes, the interval with $E_1 = E_{\mathrm{th},1}$ and $E_2 = E_{\mathrm{th},1} + 5$ MeV is used. See also the caption of Table. II.

| | $^{50}$Ca | $^{54}$Ca | $^{58}$Ca | $^{80}$Ni | $^{82}$Ni | $^{84}$Ni | $^{86}$Ni |
|---|---|---|---|---|---|---|---|
| $B(E1)$ ($e^2$ fm$^2$) | | | | | | | |
| Full pairing | 0.73 | 1.48 | 1.76 | 1.39 | 2.17 | 3.01 | 3.72 |
| No dynamical pairing | 0.64 | 1.40 | 1.72 | 1.15 | 1.86 | 2.69 | 3.41 |
| No pairing | 0.68 | 1.86 | 1.83 | 1.27 | 2.25 | 3.21 | 5.11 |

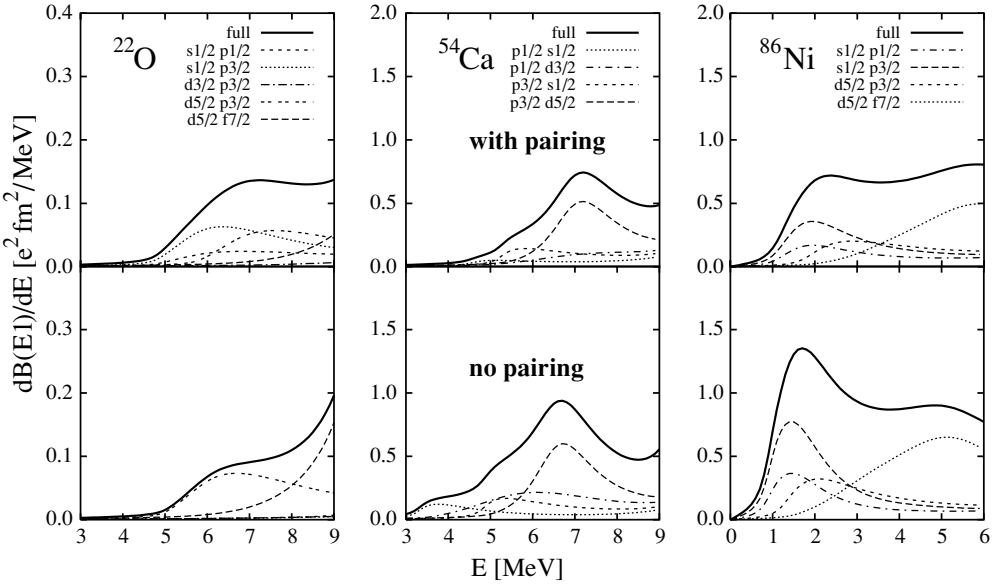


FIG. 15. Unperturbed $E1$ strength functions in $^{22}$O, $^{54}$Ca, and $^{86}$Ni. Upper panels, unperturbed strength functions obtained with the mixed pairing force; lower panels, results without the pairing correlation. Partial strengths selected by a pair of the angular momentum quantum numbers of the two-quasiparticle excitations are also plotted.

The static pairing effect in Ca and Ni isotopes appears different from that in the oxygen isotopes. For example, it causes the large suppression of the $E1$ strength in $^{86}$Ni, which is explained in terms of the neutron $3s_{1/2}$ orbit. This orbit would be fully occupied by the last two neutrons if we neglected the pair correlation (cf. Fig. 1). Since the $3s_{1/2}$ orbit is only weakly bound (the Woods-Saxon single-particle energy $e_{3s_{1/2}} = -0.78$ MeV) and has a spatially extended wave function, the particle-hole excitations from this orbit to the continuum $p$ orbits bring about a large $E1$ strength just above the one-neutron threshold energy, which is often referred to as the threshold strength (cf. the right lower panel of Fig. 15). Once the neutron pair correlation is included, the associated strength is reduced as the $3s_{1/2}$ orbit becomes partially occupied, making the contribution of the two-quasiparticle configurations $3s_{1/2} \times p^*$ to the dipole strength significantly smaller. In Ca isotopes, the unperturbed strength in the soft dipole strength is dominated by contributions of the two-quasiparticle excitations $2p_{1/2,3/2} \times d^*$ and $2p_{1/2,3/2} \times s^*$ (Fig. 15). The increase in the quasiparticle energy of the $2p_{1/2,3/2}$ state caused by the pair correlation pushes up the peak around $E \sim 7$ MeV by about 1 MeV.

We thus conclude that the static pairing effect shows variety in different nuclides, depending strongly on low-energy quasiparticle states (around the Fermi energy) which are quite sensitive to the pairing correlation. By the same token, this suggests that the unperturbed strength function associated with the soft dipole excitation would depend somehow on the particle-hole mean field, because the single-particle states will be slightly different, for example, in the cases of the Woods-Saxon potential and the Skyrme Hartree-Fock mean field.

We then look into the dynamical pairing effect. We immediately see that in contrast to the static effect, the dynamical pairing effect has a systematic tendency to increase the dipole strength in all examples shown in Fig. 14, although the magnitude of the increase varies. The effect on $B(E1)$ associated with the soft dipole excitation is shown in Tables II and III. The largest effect on $B(E1)$ amounting to 10−40% is seen in $^{18-22}$O, and ∼10−15% in the nickel isotopes. The increase of the strength due to the dynamical pairing effect is found in the previous QRPA calculations for oxygen isotopes [31,32,62]. We here find that the increase due to the dynamical pairing correlation is universally seen in spherical nuclei near the drip line in the medium mass region. Note also that the enhancement due to the dynamical pairing effect has a similarity to the pair interaction effect predicted on the soft dipole excitation in the two-neutron halo nucleus $^{11}$Li [14].

### D. Transition densities: Particle-particle dominance in the soft dipole excitation

Characters of the soft dipole excitation can be clarified by looking into the transition densities. Choosing a representative energy, we evaluate the particle-hole transition density $\rho^{\rm ph}(r)$ and particle-pair and the hole-pair transition densities $P^{\rm pp}(r)$ and $P^{\rm hh}(r)$. They are plotted in Figs. 16, 17, and 18. It is seen in the particle-hole transition density $\rho^{\rm ph}(r)$ that in the external region ($r \gtrsim R_{\rm surf}$), the soft dipole excitation has significant neutron amplitude, whereas there is essentially no amplitude for protons, indicating that only neutrons are moving in the external region. At and slightly inside the surface, the particle-hole amplitudes of neutrons and protons have the same sign, but with the opposite phase to the external neutron amplitude, indicating that both neutrons and protons in this region move coherently against the external neutron motion. The external neutron motion is responsible for the soft dipole strength. This behavior of the particle-hole transition

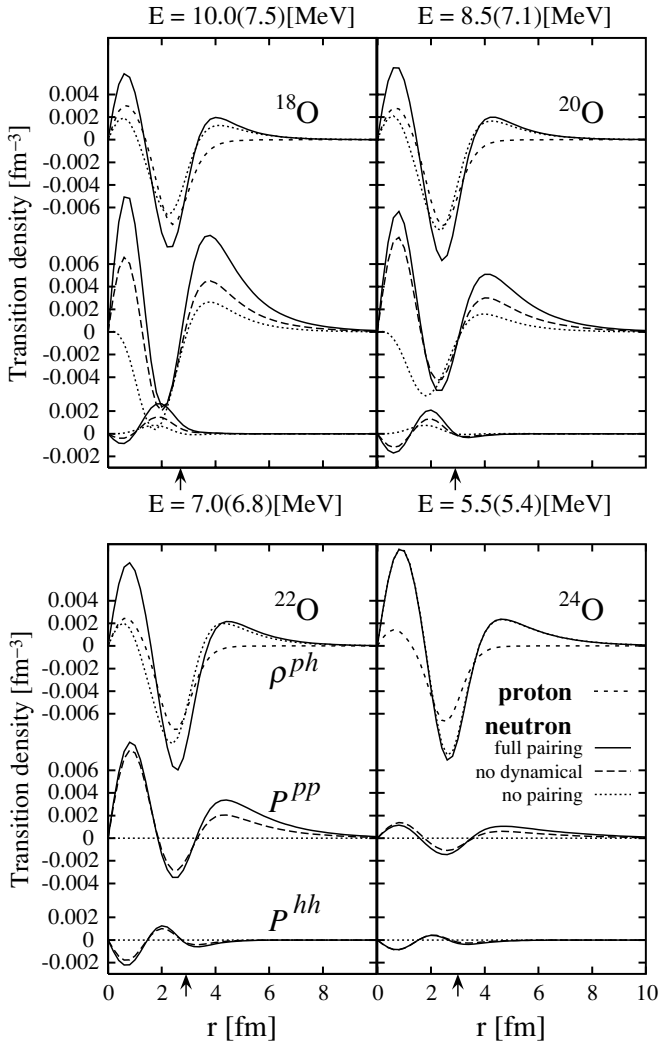


FIG. 16. Particle-hole transition density $\rho^{\rm ph}_{iqL}(r)$ (top plot in each panel), particle-pair transition density $P^{\rm pp}_{iqL}(r)$ (middle plot), and hole-pair transition density $P^{\rm hh}_{iqL}(r)$ (bottom plot) of neutrons for the soft dipole excitation in the oxygen isotopes (solid lines). Particle-hole transition density $\rho^{\rm ph}_{iqL}(r)$ of protons is also shown (dashed line with wide intervals). For the pair transition densities $P^{\rm pp}(r)$ and $P^{\rm hh}(r)$, the neutron amplitudes calculated by neglecting the dynamical pairing effect are also displayed (dashed line). Dotted lines represent the neutron transition densities calculated by neglecting all the pairing correlations. Arrow indicates the surface radius (the half-density neutron radius) $R_{\rm surf}$. The selected excitation energy is $E =$ 10.0, 8.5, 7.0, 5.5 MeV for $^{18,20,22,24}$O ($E = 7.5, 7.1, 6.8, 5.4$ MeV in the case of the no pairing calculation), which are indicated also in the figure. The $B(E1)$ value listed in Table II is used for the normalization.

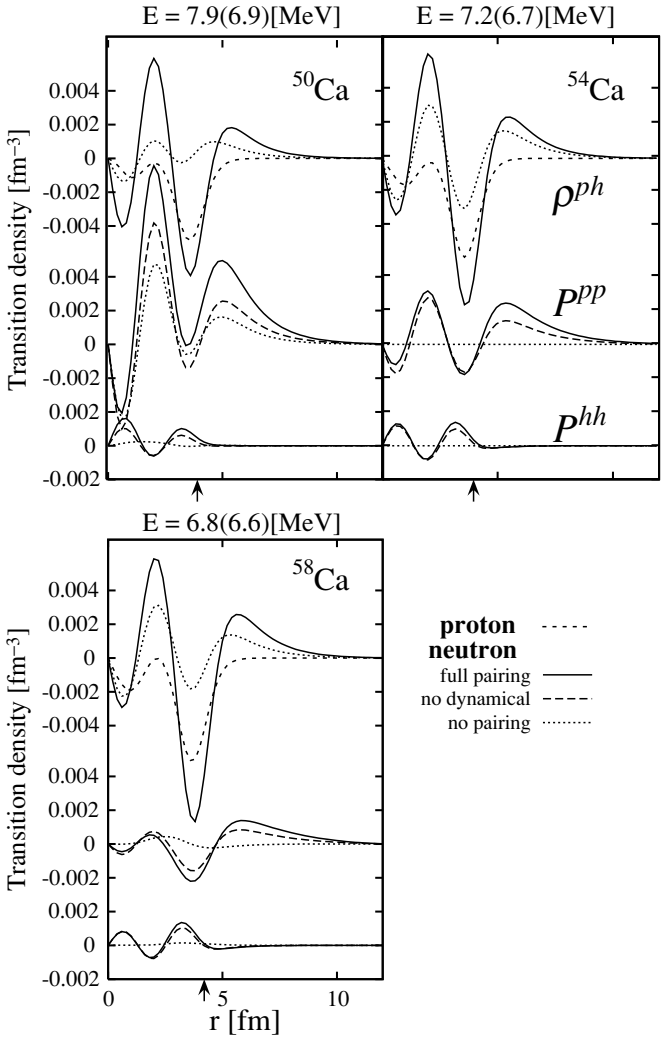


FIG. 17. Same as Fig. 16, but for the calcium isotopes. Transition densities are evaluated at the peak energy of the soft dipole excitation indicated in each panel. $E1$ strength listed in Table III is used for the normalization.

density in the soft dipole excitation is commonly seen also in other RPA and QRPA calculations without and with the pair correlations [25–27,31,32].

A novel finding in the present analysis is that the neutron particle-pair transition density $P^{\rm pp}(r)$ has very large amplitude in the external region, where the amplitude even exceeds that of the particle-hole transition density $\rho^{\rm ph}(r)$. The hole-pair transition density $P^{\rm hh}(r)$, on the other hand, is the smallest among the three transition densities and almost negligible in the external region. The relation $|P^{\rm pp}(r)| > |\rho^{\rm ph}(r)| > |P^{\rm hh}(r)|$ in the external region is seen in all isotopes in Figs. 16, 17, and 18, except in $^{24}$O and $^{58}$Ca, where $P^{\rm pp}(r)$ is still sizable. The dominance of $P^{\rm pp}(r)$ indicates that the soft dipole excitation has a character of a particle-particle excitation. It is more appropriate to characterize the soft dipole excitation as the motion of a spin-singlet neutron pair in the external region, than to describe it as a simple particle-hole excitation of a neutron to continuum states. We also note that the particle-pair transition density $P^{\rm pp}(r)$ displays a characteristic isotopic dependence. The large particle-pair amplitude in $^{50,54}$Ca and $^{18-22}$O decreases with increasing neutron number, while the particle-hole amplitude increases in the other way. A similar but slightly weak isotopic dependence is seen in the nickel isotopes.

To reveal the origin of the particle-particle dominance in the soft dipole excitation, we investigate the influence of the pairing correlations on the transition densities. Comparing

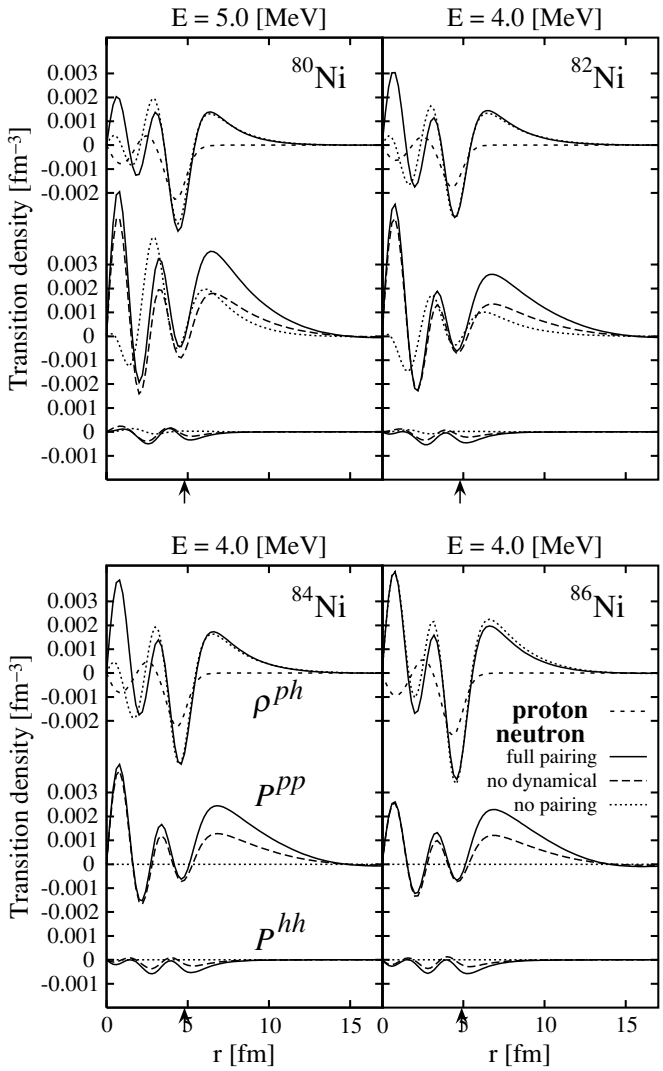


FIG. 18. Same as Fig. 16 but for the nickel isotopes. Same excitation energy is used to calculate the transition densities with and without the pairing correlation.

with calculations where the pairing effects are fully neglected (shown in Figs. 16, 17, and 18 by the dotted line), we immediately see that the neutron pair correlation brings about the large particle-pair amplitude in the exterior region $r > R_{\rm surf}$. In Figs. 16 , 17, and 18, we also show results obtained by neglecting the dynamical pairing correlation. It is seen that both the static and the dynamical pair correlations are responsible for the particle-particle dominance. In particular, the dynamical pair correlation has a dramatic influence that enhances $P^{\rm pp}(r)$ by a factor of about 2 or more in the external region. In the following, we investigate in more detail the static and dynamical effects separately.

#### *1. The static pairing effect*

Generally, low-energy two-quasiparticle excitations, which are building blocks of a low-lying excitations under the influence of a pairing correlation, carry simultaneously particle-hole, particle-pair, and hole-pair amplitudes. As an example, let us consider the neutron two-quasiparticle excitations $2s_{1/2} \times p^*$ and $1d_{5/2} \times p^*$ (and $1d_{5/2} \times f^*$), which give dominant contributions to the unperturbed strength function in $^{22}$O (cf. Fig. 15). With the pairing correlation included, the quasiparticle state $2s_{1/2}$ has a large amplitude both in the upper and lower components (corresponding to the particle and hole components, respectively) of the wave function since it is located near the Fermi energy. Accordingly, the two-quasiparticle configuration $2s_{1/2} \times p^*$ brings a large amplitude both in the particle-hole transition density $\rho^{\rm ph}(r)$ and in the particle-pair transition density $P^{\rm pp}(r)$. (The hole-pair transition density $P^{\rm hh}(r)$ is small since both $2s_{1/2}$ and $p^*$ are located above the Fermi energy, and particle characters are dominant in these quasiparticle states.) The amplitudes $P^{\rm pp}(r)$ and $\rho^{\rm ph}(r)$ associated with the configuration $2s_{1/2} \times p^*$ are especially large in the exterior region as the quasiparticle wave function of the $2s_{1/2}$ state is spatially extended to the outside. The other dominant configuration $1d_{5/2} \times p^*(f^*)$ contributes also to the particle-pair transition density in a similar way. The particle-particle character of these two-quasiparticle excitations in $^{18,20}$O decreases as the Fermi energy (the neutron number) increases. In $^{24}$O, the particle-particle character becomes small as the quasiparticle states $1d_{5/2}$ and $2s_{1/2}$ both have a dominant hole character. The qualitative trends observed in the transition densities can be connected in this way to the properties of the relevant quasiparticle states. Similar mechanisms are applied to the calcium isotopes, where the neutron $2p_{3/2,1/2}$ states play a central role. In the nickel isotopes, the relevant neutron quasiparticle states are $3s_{1/2}$ and $2d_{5/2}$ (see Figs. 1 and 15).

#### *2. The dynamical pairing effect*

It is clear that the static pairing effects discussed above explains only qualitative aspects of the transition densities since the static pairing effect alone explains about a half of the particle-pair transition amplitude. The dynamical effect adds an essential enhancement to $P^{\rm pp}(r)$, especially in the external region which is most relevant to the soft dipole excitation. The increase by a factor of 2 in the particle-pair transition amplitude $P^{\rm pp}(r)$ corresponds to an enhancement of a factor of about 4 in the strength of neutron pair transfer. Namely, the characteristic particle-pair dominance of the soft excitation is strongly affected by the RPA correlations. This means that the calculated soft dipole excitation cannot be explained as a few representative two-quasiparticle configurations which we find responsible for the static pairing effect, such as $2s_{1/2} \times p^*$ or $1d_{5/2} \times p^*(f^*)$ in the case of O isotopes. This conclusion is quite different from that of the RPA calculations neglecting the pair correlations [25,27], which predict the soft dipole excitation in neutron-rich oxygen isotopes as a noncollective independent particle-hole excitation of weakly bound neutrons. It is also noted that the large enhancement of the particle-pair transition density $P^{\rm pp}(r)$ by the dynamical pairing correlation is commonly seen in all the calculated examples in different isotope chains O, Ca, and Ni, where single-particle structures near the Fermi energy are different. This indicates that the large dynamical pairing effect is a

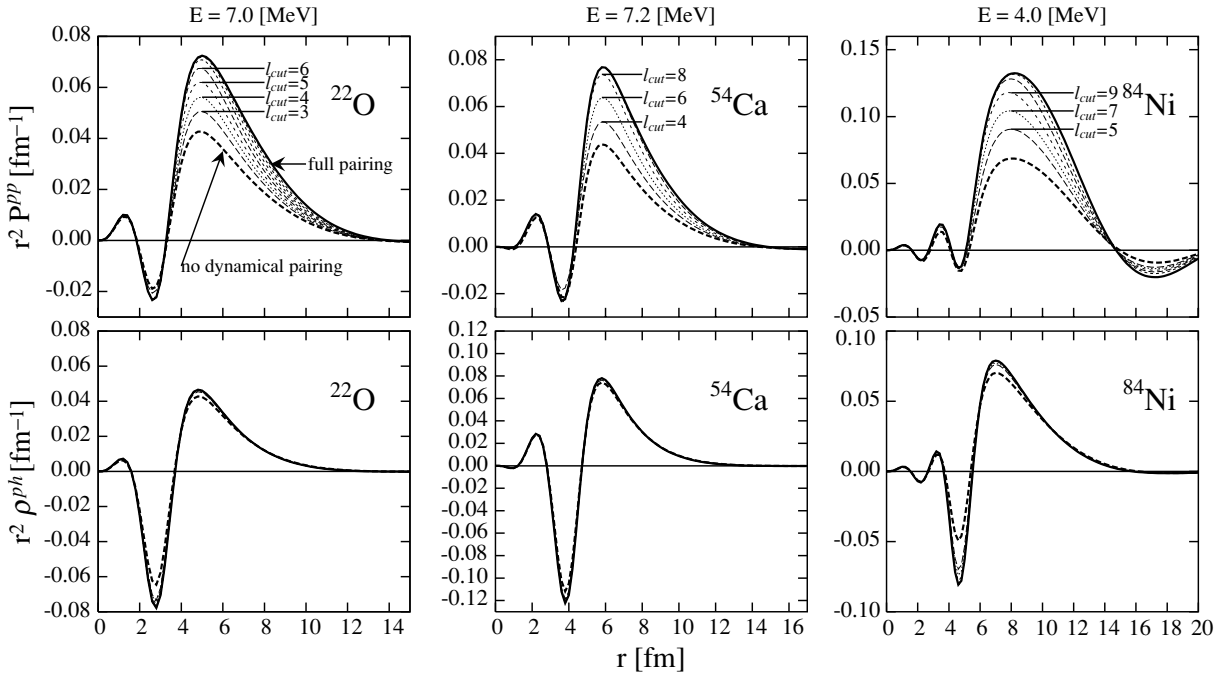


FIG. 19. Dependence of the particle-pair transition density $r^2 P^{\rm pp}(r)$ (top panels) and the particle-hole transition density $r^2\rho^{\rm ph}(r)$ (bottom panels) of neutrons on the cutoff orbital angular momentum $l_{\rm cut}$ of the neutron quasiparticle states in $^{22}$O, $^{54}$Ca, and $^{84}$Ni. The results with $l_{\rm cut} = l^0_{\rm cut}(= 3), 4, 5, \ldots, 9$ for $^{22}$O, $l_{\rm cut} = l^0_{\rm cut}(= 4), 6, 8, 10$ for $^{54}$Ca, and $l_{\rm cut} = l^0_{\rm cut}(= 5), 7, 9, 11, 13$ for $^{84}$Ni are shown by thin lines. Here the volume element $r^2$ is multiplied to magnify the amplitude in the external region. For reference, the result with the full pairing effects and the one without the dynamical pairing correlation are shown by the thick solid and the thick dashed lines, respectively.

phenomenon that is rather insensitive to details of the single-particle structure near the Fermi energy.

### E. Di-neutron correlation in the soft dipole excitation

We shall investigate the nature of the large dynamical pairing effect on the particle-pair transition density $P^{\rm pp}(r)$. The large amplitude in $P^{\rm pp}(r)$ itself indicates that the pair correlation enhances the probability to find two neutrons participating in the soft dipole excitation at the same position $\boldsymbol{r}$. It is then tempting to interpret it in connection with the di-neutron correlation which we found in the ground state. To check this viewpoint, we examine contributions of high-$l$ quasiparticle orbits to the soft dipole excitations.

We have performed calculations where the contribution of quasiparticles with high angular momenta is truncated in evaluating the RPA correlations. In practice, we put an upper cutoff $l_{\rm cut}$ to the sum the over the orbital angular momenta $l$ and $l'$ of the two quasiparticle configurations in the density response function, Eq. (15). If the pairing correlation is completely neglected, the angular momentum of quasiparticles contributing to the dipole response is limited in a small range $0 \leqslant l \leqslant l^0_{\rm cut} = l_{\rm occ} + 1$, where $l_{\rm occ}$ is the largest orbital angular momentum of the occupied bound Woods-Saxon single-particle orbits. In the case of oxygen isotopes $^{18-24}$O, for instance, neutrons would occupy $s$, $p$ and $d$ bound orbits in the ground state in the null pairing case, and hence only the angular momentum combinations $[s \times p]_{L=1}$, $[p \times d]_{L=1}$ and $[d \times f]_{L=1}$ contribute. The cutoff $l^0_{\rm cut} = 3$ is sufficient in this case. As the pairing correlation is taken into account, however, all combinations including $[l \times (l+1)]_{L=1}$ with $l \geqslant l^0_{\rm cut}$ are allowed to contribute. Note that these high-$l$ quasiparticle states are all continuum orbits.

Results of the truncated calculations are shown in Fig. 19. It is seen that contributions from neutron high-$l$ quasiparticle states with $l > l_{\rm occ}$ are essential to produce the large enhancement in the particle-particle transition density. In $^{22}$O and $^{54}$Ca, the angular momenta up to $l \sim 9$ and $l \sim 10$, respectively, are necessary to approach the final result. In $^{84}$Ni, the orbits up to $l \sim 13$ contribute in the external region up to $r \lesssim 12$ fm, but very high angular momenta $l > 13$ still continue to influence in the far outside $r \gtrsim 15$ fm. The particle-hole transition amplitude $\rho^{\rm ph}(r)$, on the other hand, is affected very little by the high-$l$ continuum configurations with $l > l_{\rm occ}$, as seen in Fig. 19.

We thus conclude that the neutron correlation responsible for the large enhancement of the particle-pair transition density $P^{\rm pp}(r)$ in the soft dipole excitation is associated with a coherent superposition of a large number of neutron two-quasiparticle configurations with angular momentum coupling $[l \times (l+1)]_{L=1}$ involving up to large values of $l$. The accumulating high-$l$ contribution can be regarded as evidence that two neutrons carrying the soft dipole mode are spatially correlated at short relative distance in such a way that we have seen the di-neutron correlation in the ground state (cf. Sec. II C). This suggests that the soft dipole excitation is characterized rather strongly by motion of a spin-singlet di-neutron in the nuclear exterior against the remaining $A - 2$ system.

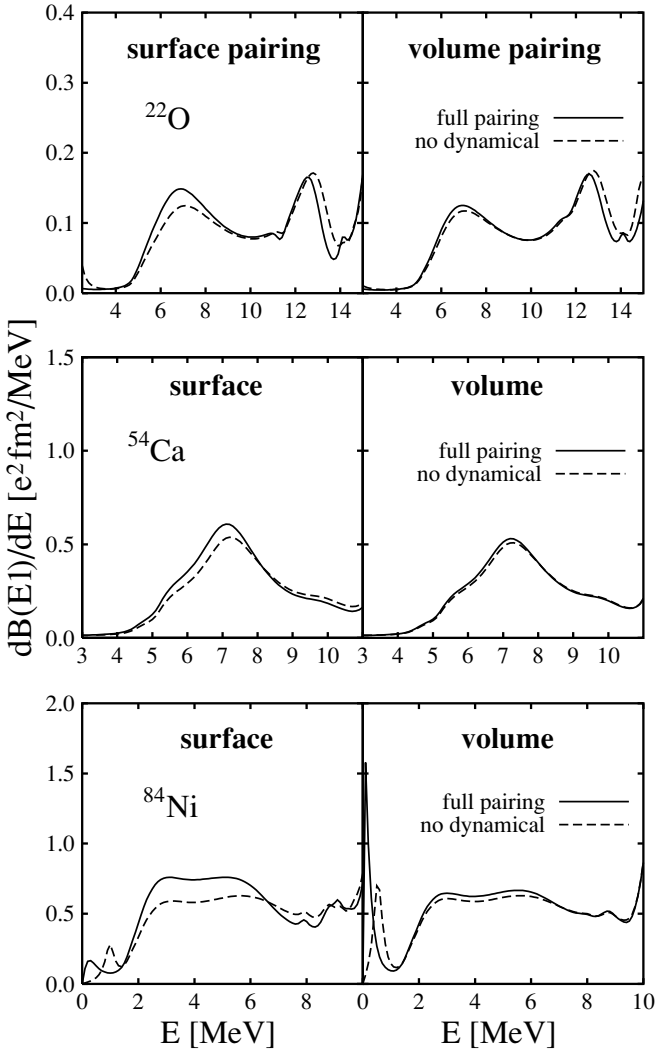


FIG. 20. $E1$ strength functions in $^{22}$O, $^{58}$Ca, and $^{84}$Ni calculated with the surface and volume pairing forces having different density dependence (solid line). Left panels show results with surface pairing with $\rho_0 = 0.19$ fm$^{-3}$, right panels are those with volume pairing. Dashed line represents results without the dynamical pairing effect. See the caption of Fig. 9 for the adopted force parameters.

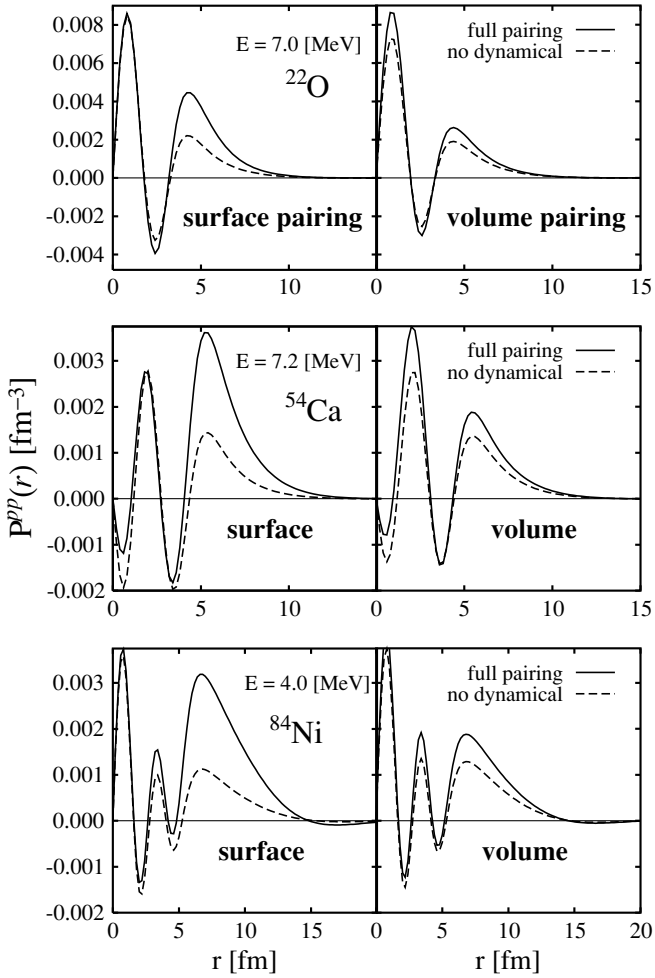


FIG. 21. Same as Fig. 20, but for the particle-pair transition density $P^{\rm pp}(r)$ of neutrons associated with the soft dipole excitation at the excitation energies indicated in the figure.

It is noted that much larger values of angular momentum contribute in the soft dipole excitation than in the ground state. In $^{84}$Ni, for example, we need angular momentum up to $l \sim 13$ to achieve an approximate convergence around $r = 7$–$12$ fm where the pair transition density has the dominant distribution. This is because the di-neutron correlation in the soft dipole excitation takes place much farther outside of the nuclear surface than that in the case of the ground state. Note also that in $^{84}$Ni, convergence of high-$l$ contributions to the particle-pair transition density $P^{\rm pp}(r)$ is slow in the very far exterior $r > 15$ fm even around the maximum angular momentum $13 \lesssim l \leqslant l_{\rm max} (= 17)$. This is related to the fact that two neutrons can escape simultaneously in the nickel isotopes where the soft dipole excitation lies above the two-neutron threshold energy $E_{\rm th,2}$. The oscillation of $P^{\rm pp}(r)$ at $r \gtrsim 10$ fm indeed indicates a sizable two-neutron escaping. The slow convergence with respect to the angular momentum at very large distances suggests that there exists the pair correlation between the two escaping neutrons.

### F. Dependence on pair interaction

Since the soft dipole excitation is strongly influenced by the neutron pairing correlation, sensitivity of the soft dipole excitation to the effective pairing force is expected. We shall examine this issue in connection with the di-neutron correlation, focusing on the density dependence of the effective pair interaction.

We performed calculations using the volume pairing (the density-independent) force and the surface pairing force with strong density-dependence as done in Sec. II. Calculated results are shown in Figs. 20 and 21, which may be compared also with those using the mixed pairing force, representing an intermediate density dependent force (cf. Figs. 14, 16, 17 and 18). Figures 20 and 21 clearly show that results are very different with different density-dependences. It is

seen that the dynamical enhancement of the particle-pair transition density $P^{\rm pp}(r)$ in the external region ($r > R_{\rm surf}$) is much larger with the surface paring force than with the mixed and the volume pairing forces (Fig. 21). This trend is also seen in the $E1$ strength (Fig. 20). In the case of the volume pairing force, on the other hand, the dynamical pairing effect on the strength function becomes almost insignificant, and even the particle-pair transition density is not strongly enhanced. Note that the neutron-neutron attraction acting in the low-density external region is proportional to the value of $V_0$, which differs as $|V_0| \approx 180, 280, 380$ MeV fm$^3$ for volume, mixed, and surface pairing forces, respectively. Thus, the above observation implies that the soft dipole excitation, especially the associated particle-pair transition density, is quite sensitive to the effective pairing force among neutrons moving in the low-density part outside the nuclear surface. This is, of course, related to the fact that the soft dipole excitation is essentially a mode carried by the correlated neutrons moving in the nuclear exterior. In addition, the strong sensitivity to the density dependence is in accord with a similar behavior of the di-neutron correlation in the ground state (cf. Fig. 9). This again supports the picture that the soft dipole excitation is strongly influenced by the neutron pairing correlation of the di-neutron type.

## IV. CONCLUSIONS

We have investigated the neutron pairing correlations and their influences on the soft dipole excitation in medium mass nuclei near the neutron drip line from the viewpoint of the di-neutron correlation.

The analysis using the two-body correlation density has revealed the presence of the spatial di-neutron correlation in the pair-correlated ground state in nuclei near the drip line. It is found that correlated neutron pairs exhibit a strong concentration of the probability of about 30–60% at short relative distances $|\boldsymbol{r} - \boldsymbol{r}'| \lesssim 2{-}3$ fm, which is much smaller than the nuclear radius. This di-neutron correlation enhances in the surface and skin regions in near-drip-line nuclei, although it also exists inside the nucleus and in stable nuclei along the isotopic chain. The di-neutron correlation originates from coherent superposition of the single-particle (quasiparticle) orbits with large orbital angular momenta, which are embedded in the continuum energy region.

We have analyzed the soft dipole excitation to search for the di-neutron correlation in this mode. It is found that the particle-pair transition density of neutrons in the soft dipole excitation is quite large outside the nuclear surface. This originates from the dynamical pairing correlation among neutrons moving in the external region, i.e., the RPA correlation for the excited state caused by the pairing interaction. Indeed the dynamical pair correlation is responsible for enhancing the particle-pair transition density by a factor of about 2 or more. This indicates that the soft dipole excitation under the influence of the neutron pairing correlation has a dominant particle-particle character, rather than an uncorrelated particle-hole excitation from a weakly bound orbit to continuum orbits. We find also that two-quasiparticle configurations $[l \times (l+1)]_{L=1}$ involving continuum high-$l$ orbits up to around $l \sim 10$ accumulate coherently to bring about the large particle-pair transition density. This strongly suggests that the di-neutron correlation occurs among neutrons participating in the soft dipole excitation. We are thus led to a picture that in the soft dipole excitation, a spin-singlet di-neutron moves outside the nucleus against the $A-2$ subsystem. Our analysis reveals also that the characteristic neutron pairing effects are sensitive to the density dependence of the effective pairing force. The influence of the neutron pairing correlation on the dipole strength is sizable, but it dose not always cause enhancement. The di-neutron correlation emerges more clearly in the particle-particle channel.

We expect that the di-neutron correlation present in the soft dipole excitation may be most easily and directly probed in the two-particle correlation among two neutrons escaping from the excited state, or in transfer of neutrons to the excited state. These processes may also be used as a probe to study the density dependence of the nuclear pairing correlations. These issues are interesting subjects for future investigations.

## ACKNOWLEDGMENTS

The authors thank K. Matsuyanagi, W. Nazarewicz, F. Barranco, E. Vigezzi, G. Gori, and N. Sandulescu for valuable discussions. They also acknowledge discussions with the members of the Japan-U.S. Cooperative Science Program "Mean-Field Approach to Collective Excitations in Unstable Medium-Mass and Heavy Nuclei." The numerical calculations were performed on the NEC SX-5 supercomputer systems at Research Center for Nuclear Physics, Osaka University, and at Yukawa Institute for Theoretical Physics, Kyoto University. This work was supported by the Grant-in-Aid for Scientific Research (No. 14540250) from the Japan Society for the Promotion of Science.

[1] D. Sackett, K. Ieki, A. Galonsky, C. A. Bertulani, H. Esbensen, J. J. Kruse, W. G. Lynch, D. J. Morrissey, N. A. Orr, B. M. Sherrill, H. Schulz, A. Sustich, J. A. Winger, F. Deák, Á. Horváth, Á. Kiss, Z. Seres, J. J. Kolata, R. E. Warner, and D. L. Humphrey, Phys. Rev. C **48**, 118 (1993).

[2] S. Shimoura, T. Nakamura, M. Ishihara, N. Inabe, T. Kobayashi, T. Kubo, R. H. Siemssen, I. Tanihata, and Y. Watanabe, Phys. Lett. **B348**, 29 (1995).

[3] M. Zinser, F. Humbert, T. Nilsson, W. Schwab, H. Simon, T. Aumann, M. J. G. Borge, L. V. Chulkov, J. Cub, Th. W. Elze, H. Emling, H. Geissel, D. Guillemaud-Mueller, P. G. Hansen, R. Holzmann, H. Irnich, B. Jonson, J. V. Kratz, R. Kulessa, Y. Leifels, H. Lenske, A. Magel, A. C. Mueller, G. Münzenberg, F. Nickel, G. Nyman, A. Richter, K. Riisager, C. Scheidenberger, G. Schrieder, K. Stelzer, J. Stroth, A. Surowiec, O. Tengblad, E. Wajda, and E. Zude, Nucl. Phys. **A619**, 151 (1997).

[4] T. Nakamura, S. Shimoura, T. Kobayashi, T. Teranishi, K. Abe, N. Aoi, Y. Doki, M. Fujimaki, N. Inabe, N. Iwasa, K. Katori, T. Kubo, H. Okuno, T. Suzuki, I. Tanihata, Y. Watanabe, A. Yoshida, and M. Ishihara, Phys. Lett. **B331**, 296 (1994).

[5] R. Palit, P. Adrich, T. Aumann, K. Boretzky, B. V. Carlson, D. Cortina, U. D. Pramanik, Th. W. Elze, H. Emling, H. Geissel, M. Hellström, K. L. Jones, J. V. Kratz, R. Kulessa, Y. Leifels, A. Leistenschneider, G. Münzenberg, C. Nociforo, P. Reiter, H. Simon, K. Sümmerer, and W. Walus, Phys. Rev. C **68**, 034318 (2003).

[6] T. Nakamura, N. Fukuda, T. Kobayashi, N. Aoi, H. Iwasaki, T. Kubo, A. Mengoni, M. Notani, H. Otsu, H. Sakurai, S. Shimoura, T. Teranishi, Y. X. Watanabe, K. Yoneda, and M. Ishihara, Phys. Rev. Lett. **83**, 1112 (1999).

[7] U. D. Pramanik, T. Aumann, K. Boretzky, B. V. Carlson, D. Cortina, Th. W. Elze, H. Emling, H. Geissel, A. Grünschloß, M. Hellström, S. Ilievski, J. V. Kratz, R. Kulessa, Y. Leifels, A. Leistenschneider, E. Lubkiewicz, G. Münzenberg, P. Reiter, H. Simon, K. Sümmerer, E. Wajda, and W. Walus, Phys. Lett. **B551**, 63 (2003).

[8] T. Aumann, D. Aleksandrov, L. Axelsson, T. Baumann, M. J. G. Borge, L. V. Chulkov, J. Cub, W. Dostal, B. Eberlein, Th. W. Elze, H. Emling, H. Geissel, V. Z. Goldberg, M. Golovkov, A. Grünschloß, M. Hellström, K. Hencken, J. Holeczek, R. Holzmann, B. Jonson, A. A. Korshenninikov, J. V. Kratz, G. Kraus, R. Kulessa, Y. Leifels, A. Leistenschneider, T. Leth, I. Mukha, G. Münzenberg, F. Nickel, T. Nilsson, G. Nyman, B. Petersen, M. Pfützner, A. Richter, K. Riisager, C. Scheidenberger, G. Schrieder, W. Schwab, H. Simon, M. H. Smedberg, M. Steiner, J. Stroth, A. Surowiec, T. Suzuki, O. Tengblad, and M. V. Zhukov, Phys. Rev. C **59**, 1252 (1999).

[9] A. Leistenschneider, T. Aumann, K. Boretzky, D. Cortina, J. Cub, U. D. Pramanik, W. Dostal, Th. W. Elze, H. Emling, H. Geissel, A. Grünschloß, M. Hellstr, R. Holzmann, S. Ilievski, N. Iwasa, M. Kaspar, A. Kleinböhl, J. V. Kratz, R. Kulessa, Y. Leifels, E. Lubkiewicz, G. Münzenberg, P. Reiter, M. Rejmund, C. Scheidenberger, C. Schlegel, H. Simon, J. Stroth, K. Sümmerer, E. Wajda, W. Walús, and S. Wan, Phys. Rev. Lett. **86**, 5442 (2001).

[10] E. Tryggestad, T. Baumann, P. Heckman, M. Thoennessen, T. Aumann, D. Bazin, Y. Blumenfeld, J. R. Beene, T. A. Lewis, D. C. Radford, D. Shapira, R. L. Varner, M. Chartier, M. L. Halbert, and J. F. Liang, Phys. Rev. C **67**, 064309 (2003).

[11] A. Ozawa, O. Bochkarev, L. Chulkov, D. Cortina, H. Geissel, M. Hellström, M. Ivanov, R. Janik, K. Kimura, T. Kobayashi, A. A. Korsheninnikov, G. Münzenberg, F. Nickel, Y. Ogawa, A. A. Ogloblin, M. Pfützner, V. Pribora, H. Simon, B. Sitár, P. Strmen, K. Sümmerer, T. Suzuki, I. Tanihata, M. Winkler, and K. Yoshida, Nucl. Phys. **A691**, 599 (2001).

[12] H. Sagawa, N. Van Giai, N. Takigawa, M. Ishihara, and K. Yazaki, Z. Phys. A **351**, 385 (1995).

[13] F. Catara, C. H. Dasso, and A. Vitturi, Nucl. Phys. **A602**, 181 (1996).

[14] G. F. Bertsch and H. Esbensen, Ann. Phys. (NY) **209**, 327 (1991); H. Esbensen and G. F. Bertsch, Nucl. Phys. **A542**, 310 (1992).

[15] K. Ikeda, INS Report JHP-7, 1988; Nucl. Phys. **A538**, 355c (1992).

[16] M. V. Zhukov, B. V. Danilin, D. V. Fedorov, J. M. Bang, I. J. Thompson, and J. S. Vaagen, Phys. Rep. **231**, 151 (1993).

[17] F. Barranco, P. F. Bortignon, R. A. Broglia, G. Colò, and E. Vigezzi, Eur. Phys. J. A **11**, 385 (2001).

[18] S. Aoyama, K. Katō, and K. Ikeda, Prog. Theor. Phys. Suppl. **142**, 35 (2001); T. Myo, S. Aoyama, K. Katō, and K. Ikeda, Prog. Theor. Phys. **108**, 133 (2002).

[19] R. H. Ibarra, N. Austern, M. Vallieres, and D. H. Feng, Nucl. Phys. **A288**, 397 (1977).

[20] F. A. Janouch and R. J. Liotta, Phys. Rev. C **27**, 896 (1983).

[21] F. Catara, A. Insolia, E. Maglione, and A. Vitturi, Phys. Rev. C **29**, 1091 (1984).

[22] L. Ferreira, R. Liotta, C. H. Dasso, R. A. Broglia, and A. Winther, Nucl. Phys. **A426**, 276 (1984).

[23] P. G. Hansen and B. Jonson, Europhys. Lett. **4**, 409 (1987); Nucl. Phys. **A632**, 383 (1998).

[24] B. V. Danilin, I. J. Thompson, J. S. Vaagen, and M. V. Zhukov, Nucl. Phys. **A632**, 383 (1998).

[25] F. Catara, E. G. Lanza, M. A. Nagarajan, and A. Vitturi, Nucl. Phys. **A624**, 449 (1997).

[26] I. Hamamoto, H. Sagawa, and X. Z. Zhang, Phys. Rev. C **57**, R1064 (1998); Nucl. Phys. **A648**, 203 (1999).

[27] D. Vretenar, N. Paar, P. Ring, and G. A. Lalazissis, Nucl. Phys. **A692**, 496 (2001).

[28] H. Sagawa and T. Suzuki, Phys. Rev. C **59**, 3116 (1999).

[29] G. Colò and P. F. Bortignon, Nucl. Phys. **A696**, 427 (2001).

[30] S. Goriely and E. Khan, Nucl. Phys. **A706**, 217 (2002).

[31] M. Matsuo, Prog. Theor. Phys. Suppl. **146**, 110 (2002).

[32] N. Paar, P. Ring, T. Niksic, and D. Vretenar, Phys. Rev. C **67**, 034312 (2003).

[33] S. Goriely, E. Khan, and M. Samyn, Nucl. Phys. **A739**, 331 (2004).

[34] D. Sarchi, P. F. Bortignon, and G. Colò, Phys. Lett. **B601**, 27 (2004).

[35] J. Dobaczewski, H. Flocard, and J. Treiner, Nucl. Phys. **A422**, 103 (1984).

[36] A. Bulgac, preprint FT-194-1980, nucl-th/9907088.

[37] J. Dobaczewski, W. Nazarewicz, T. R. Werner, J. F. Berger, C. R. Chinn, and J. Dechargé, Phys. Rev. C **53**, 2809 (1996).

[38] J. Dobaczewski, W. Nazarewicz, and P.-G. Reinhard, Nucl. Phys. **A693**, 361 (2001).

[39] J. Dobaczewski and W. Nazarewicz, Prog. Theor. Phys. Suppl. **146**, 70 (2002); J. Dobaczewski, W. Nazarewicz, and M. V. Stoitsov, Euro. Phys. J. A **15**, 21 (2002).

[40] M. Grasso, N. Sandulescu, Nguyen Van Giai, and R. J. Liotta, Phys. Rev. C **64**, 064321 (2001).

[41] M. V. Stoitsov, J. Dobaczewski, W. Nazarewicz, S. Pittel, and D. J. Dean, Phys. Rev. C **68**, 054312 (2003).

[42] E. Terán, V. E. Oberacker, and A. S. Umar, Phys. Rev. C **67**, 064314 (2003).

[43] Yongle Yu and A. Bulgac, Phys. Rev. Lett. **90**, 222501 (2003).

[44] P. Ring and P. Schuck, *The Nuclear Many-Body Problem* (Springer-Verlag, Berlin, 1980).

[45] J.-P. Blaizot and G. Ripka, *Quantum Theory of Finite Systems* (MIT, Cambridge, MA, 1986).

[46] J. Engel, M. Bender, J. Dobaczewski, W. Nazarewicz, and R. Surman, Phys. Rev. C **60**, 014302 (1999).

[47] M. Bender, J. Dobaczewski, J. Engel, and W. Nazarewicz, Phys. Rev. C **65**, 054322 (2002).

[48] M. Matsuo, Nucl. Phys. **A696**, 371 (2001).

[49] E. Khan, N. Sandulescu, M. Grasso, and N. V. Giai, Phys. Rev. C **66**, 024309 (2002).

[50] E. Khan, N. Sandulescu, N. V. Giai, and M. Grasso, Phys. Rev. C **69**, 014314 (2004).
[51] M. Yamagami and N. V. Giai, Phys. Rev. C **69**, 034301 (2004); M. Yamagami, *Proceedings of the Fifth Japan-China Joint Nuclear Symposium*, March 7–10, 2004, Japan, preprint nucl-th/0404030.
[52] J. Terasaki, J. Engel, M. Bender, J. Dobaczewski, W. Nazarewicz, and M. Stoitsov, Phys. Rev. C **71**, 034310 (2005).
[53] D. Vretenar, N. Paar, T. Nikšić, and P. Ring, Phys. Rev. Lett. **91**, 262502 (2003).
[54] N. Paar, T. Nikšić, D. Vretenar, and P. Ring, Phys. Rev. C **69**, 054303 (2004).
[55] S. Shlomo and G. Bertsch, Nucl. Phys. **A243**, 507 (1975).
[56] G. F. Bertsch and S. F. Tsai, Phys. Rep. **18**, 125 (1975).
[57] G. A. Bartholomew, E. D. Earle, A. J. Feguson, J. W. Knowles, and M. A. Lone, *Advances in Nuclear Physics*, edited by M. Baranger and E. Vogt (Plenum, New York, 1972), Vol. 7, p. 229.
[58] M. Igashira, H. Kitazawa, M. Shimizu, H. Komano, and N. Yamamuro, Nucl. Phys. **A457**, 301 (1986).
[59] Y. Suzuki, K. Ikeda, and H. Sato, Prog. Theor. Phys. **83**, 180 (1990).
[60] D. Vretenar, N. Paar, P. Ring, and G. A. Lalazissis, Phys. Rev. C **63**, 047301 (2001).
[61] N. Ryezayeva, T. Hartmann, Y. Kalmykov, H. Lenske, P. von Neumann-Cosel, V. Yu. Ponomarev, A. Richter, A. Shevchenko, S. Volz, and J. Wambach, Phys. Rev. Lett. **89**, 272502 (2002).
[62] M. Matsuo, K. Mizuyama, and Y. Serizawa, in *Proceedings of the International Symposium on Frontiers of Collective Motions*, edited by H. Sagawa and H. Iwasaki (World Scientific, Singapore, 2003) p. 312; M. Matsuo, in *Proceedings of the International Symposium "A New Era of Nuclear Structure Physics,"* edited by Y. Suzuki, S. Ohya, M. Matsuo, and T. Ohtsubo (World Scientific, Singapore, 2004), p. 246.
[63] R. R. Chasman, Phys. Rev. C **14**, 1935 (1976).
[64] J. Terasaki, P.-H. Heenen, P. Bonche, J. Dobaczewski, and H. Flocard, Nucl. Phys. **A593**, 1 (1995).
[65] E. Garrido, P. Sarriguren, E. Moya de Guerra, and P. Schuck, Phys. Rev. C **60**, 064312 (1999).
[66] M. Yamagami, K. Matsuyanagi, and M. Matsuo, Nucl. Phys. **A693**, 579 (2001).
[67] W. Satuła, J. Dobaczewski, and W. Nazarewicz, Phys. Rev. Lett. **81**, 3599 (1998).
[68] N. Fukunishi, T. Otsuka, and I. Tanihata, Phys. Rev. C **48**, 1648 (1993).
[69] I. Hamamoto and X. Z. Zhang, Phys. Rev. C **52**, R2326 (1995).
[70] D. M. Brink, in *Proceedings of the International Symposium on Frontiers of Collective Motions*, edited by H. Sagawa and H. Iwasaki (World Scientific, Singapore, 2003) p. 210.
[71] E. Chabanat, P. Bonche, P. Haensel, J. Meyer, and R. Schaeffer, Nucl. Phys. **A635**, 231 (1998); **A643**, 441 (1998).
[72] J. Bardeen, L. N. Cooper, and J. R. Schrieffer, Phys. Rev. **108**, 1175 (1957); P. G. de Gennes, *Superconductivity of Metals and Alloys* (Benjamin, New York, 1966); M. Tinkham, *Introduction to Superconductivity* (McGraw-Hill, New York, 1975).
[73] A. Bohr and B. R. Mottelson, *Nuclear Structure* (Benjamin, New York, 1975), Vol. 2.
[74] F. Barranco, R. A. Broglia, H. Esbensen, and E. Vigezzi, Phys. Rev. C **58**, 1257 (1998).
[75] J. Dechargé and D. Gogny, Phys. Rev. C **21**, 1568 (1980).
[76] S. T. Belyaev, A. V. Smirnov, S. V. Tolokonnikov, and S. A. Fayans, Sov. J. Nucl. Phys. **45**, 783 (1987).